

Geometric shape matching for recovering protein conformations from single-particle Cryo-EM data *

Erik Jansson [†], Jonathan Krook [‡], Klas Modin [§], and Ozan Öktem [¶]

Abstract. We address recovery of the three-dimensional backbone structure of single polypeptide proteins from single-particle cryo-electron microscopy (Cryo-SPA) data. Cryo-SPA produces noisy tomographic projections of electrostatic potentials of macromolecules. From these projections, we use methods from shape analysis to recover the three-dimensional backbone structure. Thus, we view the reconstruction problem as an indirect matching problem, where a point cloud representation of the protein backbone is deformed to match 2D tomography data. The deformations are obtained via the action of a matrix Lie group. By selecting a deformation energy, the optimality conditions are obtained, which lead to computational algorithms for optimal deformations. We showcase our approach on synthetic data, for which we recover the three-dimensional structure of the backbone.

Key words. Inverse problems, Tomography, Regularization, Shape analysis, Manifold-valued data, Optimization, Lie groups, Electron microscopy, Single particle analysis, Cryogenic electron microscopy

MSC codes. 53Z50, 90C26, 68U10, 53Z10, 92C55

1. Introduction. Biological macromolecular complexes (biomolecules), like proteins and nucleic acids, form the molecular machinery that sustains both life and disease. An essential part of biomedical research is therefore to understand the functionality of biomolecules, for example to design an antiviral drug as a protease that blocks the “spike” protein which binds the SARS-CoV-2 virus to our cells. Similarly, mRNA vaccines consist of nucleic acids in a large lipid nanoparticle that results in the synthesis of antibodies.

1.1. Structures of biomolecules. The functionality of a biomolecule, in particular of a protein, is largely governed by the dynamics of its 3D shape (structure). Structural biology focuses on developing experimental and computational methods for determining the structure and dynamics of biomolecules.

Historically, the structure of proteins has been obtained through X-ray crystallography. As the name suggests, the approach requires one to crystallize the protein. One can then experimentally measure X-ray scattering data from such crystals. Computational methods (phase recovery) combined with experimental protocols are then used to recover the 3D electron density function of the protein from the scattering data. The final step is to fold the

***Funding:** This work was funded by the Wallenberg AI, Autonomous Systems and Software Program (WASP), the Knut and Alice Wallenberg Foundation grant WAF2019.0201, and the Swedish Research Council grants 2020-03107 and 2022-03453.

[†]erikjans@chalmers.se, DEPARTMENT OF MATHEMATICAL SCIENCES, CHALMERS UNIVERSITY OF TECHNOLOGY AND GOTHENBURG UNIVERSITY, GOTHENBURG, SWEDEN

[‡]jkroo@kth.se, DEPARTMENT OF MATHEMATICS, KTH - ROYAL INSTITUTE OF TECHNOLOGY, STOCKHOLM, SWEDEN

[§]klas.modin@chalmers.se, DEPARTMENT OF MATHEMATICAL SCIENCES, CHALMERS UNIVERSITY OF TECHNOLOGY AND GOTHENBURG UNIVERSITY, GOTHENBURG, SWEDEN

[¶]ozan@kth.se, DEPARTMENT OF MATHEMATICS, KTH - ROYAL INSTITUTE OF TECHNOLOGY, STOCKHOLM, SWEDEN

primary structure of the protein (which can be determined from the gene sequence that codes for its synthesis) into the recovered 3D electron density function. This step is fairly straightforward if the density function has sufficient 3D resolution and the folding yields an atomic model of the protein (structure).

X-ray crystallography has been widely successful, and it is currently the standard approach in structural biology for protein structure determination. It is, however, limited to biomolecules that can be crystallized. Furthermore, the approach is designed for recovering a single static structure¹. In particular, recovering structural dynamics of biomolecules in tissue (in-situ) or aqueous solution (in-vitro) remains an open problem. Development of experimental and computational methods for this purpose is therefore an active research area. A promising approach is based on 3D electron microscopy, which we consider next.

1.2. 3D electron microscopy. Structural biology has in the last decade undergone a revolution with a new generation of computational and experimental methods for recovery and analysis of biomolecular structures. Most notably is the development of methods based on transmission electron microscope (TEM) imaging.

The idea to combine principles from tomography with TEM imaging to recover 3D structures of biomolecules can be traced back to [73], which estimated the 3D map of a biomolecule (bacteriophage T4 tail) by taking advantage of its symmetry. Since then, the field of 3D electron microscopy has developed along several directions, and most notably towards methods for structural studies of biomolecules that lack specific symmetries.

A key difficulty in using tomographic principles for 3D electron microscopy is to obtain the necessary amount of 2D TEM images of the biomolecule from sufficiently many different views. This is possible for vitrified specimens that consist of many isolated (structurally identical) copies of the biomolecule in varying orientations. Single-particle cryo-electron microscopy (Cryo-SPA) is a 3D electron microscopy technique that is specifically designed for such data. It was introduced in [38, 52, 89, 51] and has, as surveyed in, undergone much progress regarding computational methods [4, 65, 26, 17, 80, 25, 82, 83, 9, 10], sample preparation [58, 91, 23], and instrumentation [37, 93]. This development was recognized through the 2017 Nobel Prize in Chemistry, and it has turned Cryo-SPA into a major tool in structural biology for studying large rigid biomolecules (homogenous particles) at (near) atomic resolution [24, 63, 53] that are difficult or impossible to crystallize. This is essential for both life science research [64] and drug discovery [69, 71].

Sample preparation and data acquisition. The starting point in Cryo-SPA is to prepare an aqueous solution that contains many instances of the biomolecule of interest. Each instance is referred to as a *particle*. Cryofixation is then applied to the solution, resulting in a thin, solid slab of vitrified ice. The method was first introduced in [32, 2] as a technique to solidify a specimen that avoids introducing additional unwanted heavy-metal stains or other contrast enhancements.

The vitrified slab is then imaged in a TEM where high-energy electrons scatter against the specimen in vacuum, resulting in several large 2D phase contrast TEM images (micrographs). Scattering properties of particles in the slab are modelled by the *3D map*, which is a real-

¹There are approaches, like time-resolved crystallography, that attempt to use X-ray crystallography to recover a dynamically evolving structure.

valued function on \mathbb{R}^3 that represents the electrostatic potential generated by the particle and its surrounding aqueous medium (another related function is the electron density map).

Image processing techniques (particle picking) are then used to extract 2D image patches (particle images) from these micrographs that represent a (noisy) 2D “projection image” of a *single* particle.

Computational steps. Recovering the 3D map of a particle from its corresponding single 2D particle image is not feasible, so a key assumption in Cryo-SPA is that *all* particles are copies of the *same (isolated) biomolecule*.

For a rigid biomolecule, all particles have (approximately) identical 3D structure (*homogeneous particles*). One can then use tomographic reconstruction techniques to computationally recover the 3D map for the biomolecule (*3D map estimation*), but this requires one to address the challenge that each particle has an unknown 3D orientation/translation w.r.t. the TEM optical axis (*pose*).

An additional challenge in 3D map estimation is that the 2D TEM images have *extremely low signal-to-noise ratio*, e.g., the power of the noise can easily be ten times higher than the signal. One reason is that vitrified biological specimens act as weak phase contrast objects when imaged in a TEM, so resulting images have very low contrast. Furthermore, such specimens are sensitive to radiation damage, so TEM images need to be acquired using a low dose (200–400 electrons/nm²).

A further challenge arises when the biomolecule is flexible, so particles have varying 3D structure (*heterogeneous particles*) that represent different conformations of the biomolecule. Alongside handling unknown poses, one now needs to recover a dynamical 3D map, which is significantly more challenging.

The final step is *model building*, which refers to building (pseudo) atomic models for the particles. This is an essential part of using Cryo-SPA in biological research, since interpretation and identification of biological functionality often relies on having access to (pseudo) atomic models. If the particle is a single protein, then this translates into the task of “folding” the primary structure of the protein (which is known) into the particle specific 3D map. This is in principle possible if the 3D map has sufficient resolution (about 0.4 nm or better), but the process is semi-automatic, and it requires a large degree of human intervention. Estimating the 3D map with such high resolution from Cryo-SPA data is only reachable for biomolecules that are rigid (no dynamics) [63, 13], so *model building remains an open challenge for flexible biomolecules* (heterogeneous particles).

1.3. Shape matching applied to Cryo-EM. The idea proposed in this paper is to use *geometric shape analysis*, and in particular shape matching, to model similarity of flexible proteins.

In essence, shape analysis concerns finding the energy-minimizing way to *deform* an initial shape (template) to a target shape. The framework was developed by Grenander and others in the context of *computational anatomy* (cf. [44, 45]). It has had various applications, like in medical imaging to characterize, find, or understand disease via abnormal anatomical deformations of organs such as the brain or the lungs [19, 70]. Mathematically, new shapes are obtained by deforming a template. The deformation is often modelled by the action of a group of diffeomorphisms. In its abstract setting, e.g., as presented by [15], the theory allows the

deformations to be generated by other means than diffeomorphisms. More specifically, general shape changes are obtained by letting a Lie group act on a “space of shapes”, which can be, e.g., points, curves, surfaces, volumetric maps, or combinations thereof. *Shape matching* then consists of deforming a template shape so that it matches a target shape, by minimizing a user-defined matching energy. For more information on shape matching, including the underlying mathematical theory, see the book by Younes [94] and references therein.

3D map estimation and model building in Cryo-SPA involve solving several coupled inverse problems. As we show next, these can under some additional assumptions be merged and viewed as variants of shape matching.

1.3.1. Data. Data in Cryo-SPA consists of 2D TEM images that represent the image of a single particle (particle images). Such 2D images are acquired by applying particle picking to one or more TEM micrographs.

The data consists of digitized 2D TEM images. Mathematically, one can view such 2D images as elements $y_1, \dots, y_m \in Y$ where Y (data space) is the vector space of \mathbb{R} -valued \mathcal{L}^2 -functions on \mathbb{R}^2 (detector plane). These images have, as already mentioned, very low contrast (vitrified biological specimens act as phase contrast object) and high noise level (and such specimens need to be imaged with a very low electron dose). As a result, data in Cryo-SPA has very low signal-to-noise ratio.

1.3.2. 3D map estimation. The *task* in 3D map estimation is to reconstruct 3D maps $p_1, \dots, p_m \in X$ of the particles from corresponding data $y_1, \dots, y_m \in Y$. Elements in the set X (reconstruction space) represent 3D maps, so X is the vector space of \mathbb{C} -valued \mathcal{L}^2 -functions on \mathbb{R}^3 with rapid decay. Under additional assumptions, one can assume that the real and imaginary parts of these are proportional [66, section 4]. With this additional assumption, elements in X can be viewed as real-valued functions on \mathbb{R}^3 with rapid decay.

To proceed, we view each $y_i \in Y$ as a single sample of a Y -valued random variable y_i defined as

$$(1.1) \quad y_i := \mathcal{A}(\phi_i \cdot p_i) + \mathbf{e}_i \quad \text{with unknown pose } \phi_i \in G \text{ for } i = 1, \dots, m.$$

Here, \mathbf{e}_i is a Y -valued random variable modelling observation noise in the TEM micrograph and $\phi_i \in G$ parametrizes the pose of the i :th particle. More specifically, the pose of the particle is modelled by acting with the group G on X as $G \times X \ni (\phi, p) \mapsto \phi \cdot p \in X$. A common choice is $G := \text{SE}(3)$ with the natural action $\phi \cdot p := p \circ \phi^{-1}$, but it is enough to consider $G := \text{SO}(3)$ if the particle picking process includes “centering” the particle (which is often the case). Finally, the operator $\mathcal{A}: X \rightarrow Y$ models TEM image formation in the absence of noise. Under certain assumptions (weak phase object approximation), which hold in Cryo-SPA, one can approximate \mathcal{A} with a parallel beam ray transform along the TEM optical axis followed by a 2D convolution in the detector plane (optics CTF), see [36, 74] and [66, section 4] for details.

We can now formalize 3D map estimation as the inverse problem of *reconstructing particle specific 3D maps* $p_1, \dots, p_m \in X$ from data $y_1, \dots, y_m \in Y$. As already stated, it is not possible to recover the 3D map $p_i \in X$ from the 2D map $y_i \in Y$ *independently* for each $i = 1, \dots, m$. To proceed, one needs to utilize the assumption that *all* particles p_i originate from the *same* biomolecule. This gives rise to two possible generative models for the particles:

Homogenous particles: All particles have (approximately) identical 3D maps, so

$$(1.2) \quad p_i := x^* \quad \text{in (1.1) for } i = 1, \dots, m,$$

where $x^* \in X$ is the (true unknown) 3D map of the biomolecule and $\phi_i \in G$ is the particle-specific pose.

Heterogenous particles: Particles have differing 3D maps, but they all represent the same biomolecule. Formalizing this, we assume

$$(1.3) \quad p_i := \mathcal{W}(\psi_i, x^*) \quad \text{in (1.1) for } i = 1 \dots, m.$$

Here, $x^* \in X$ is the unknown 3D map of the biomolecule in some “ground state” and $\mathcal{W}: \mathfrak{X} \times X \rightarrow X$ models non-rigid deformations of 3D maps that are parametrized by $\psi \in \mathfrak{X}$. As an example, let \mathfrak{X} be a Lie (sub)group of diffeomorphisms on \mathbb{R}^3 and define \mathcal{W} as an appropriate \mathfrak{X} -action on X , e.g., $\mathcal{W}(\psi, p) := p \circ \psi^{-1}$ for $p \in X$ and $\psi \in \mathfrak{X}$.

A key challenge in applying tomographic reconstruction to Cryo-SPA data is to handle the extremely low signal-to-noise ratio in the 2D TEM images (subsection 1.3.1). One needs many (tens of thousands) such images of the biomolecule in varying poses. If these poses are estimated sufficiently accurately, then 3D map estimation can be performed with standard reconstruction methods from tomography, see e.g., [39, chapter 5] or the surveys [17, 84]. Pose estimation is, however, challenging when signal-to-noise ratio in data is small. Much of the development of computational methods for Cryo-SPA is catalyzed by the need to address this challenge. A key step was provided by the projection-matching methods introduced in [68, 5]. These are iterative schemes (refinement) that alternate between pose and 3D map estimation, and many variants were developed as surveyed in [80, 65]. The next major development of refinement schemes came with the introduction of maximum likelihood methods [79], which can be viewed as statistical variants of refinement where pose estimation is replaced with marginalization over poses. This addressed some of the reliability issues that plagued pose estimation part of projection-matching in high-noise regimes [81]. Despite their success, the 3D map estimation part of maximum likelihood methods had limitations. Bayesian methods introduced in [76, 75] improved upon that by accounting for 3D map priors. Nowadays, such methods are state-of-the-art for pose estimation and 3D map estimation in Cryo-SPA.

1.3.3. Model building. Model building is an essential step in structural biology that facilitates interpretation of structural data obtained by different methods, including macromolecular x-ray crystallography and Cryo-SPA. The task in Cryo-SPA is to assemble a (pseudo) atomic model from a 3D map.

One can formalize model building as an inverse problem. To achieve that, let A denote the set of possible (pseudo) atomic models that a given biomolecule can have. Next, let $\mathcal{B}: A \rightarrow X$ be the map that associates a 3D map to a (pseudo) atomic model. See [74, Appendix B] for how to construct A for simulating TEM images. Model building can now be formulated as the inverse problem of estimating a (pseudo) atomic model $v^* \in A$ from a 3D map $p \in X$, which is a single sample of the X -valued random variable \mathbf{p} defined by

$$(1.4) \quad \mathbf{p} := \mathcal{B}(v^*) + \Delta \mathbf{p}.$$

Here, Δp is the X -valued random variable representing errors in the 3D map.

A challenge is that the mapping \mathcal{B} in (1.4) is often non-injective, so model building is an ill-posed inverse problem. Many methods were originally designed for interpretation of 3D electron density maps recovered from x-ray crystallography data. The focus in these methods has been on tools for moving and refining one, or a small number of, residues, or ligands. The same principles can be used for model building of 3D maps from Cryo-SPA, so the aforementioned tools from x-ray crystallography were extended into that setting [14, 62, 59, 18, 61]. These tools are mostly designed for medium/high-resolution (0.25–0.4 nm) 3D maps [27].

There are significant challenges in fully automating the model building step in Cryo-SPA, and especially so for proteins that lack accurate homologous or predicted structures as templates (de novo model building) [40, 98]. This has catalyzed the development of various deep learning-based approaches [78, 50, 95, 49, 41, 28, 40, 55, 87, 96] along with curated data sets for training and testing such methods [42].

1.3.4. Joint 3D reconstruction and model building. The common approach is to first perform 3D map estimation, then use the resulting 3D map(s) as input to model building. Both steps involve solving ill-posed inverse problems, so usage of appropriate priors is essential for obtaining reliable and sufficiently accurate solutions.

The drawback with the above sequential approach is that it becomes difficult to make the best use of the a priori information. More precisely, most of the a priori information about the structures of biomolecules and their dynamics is in the form of biophysical constraints that apply to (pseudo) atomic models. These priors apply to model building, but performance is expected to improve if one can also use (some of) them in 3D map estimation. This is possible if one replaces the sequential approach with a joint one, where 3D map estimation is performed jointly with model building.

The inverse problem associated with joint 3D map estimation and model building is essentially a fusion of the inverse problems in (1.1) and (1.4).

Homogeneous particles: The task is to estimate the unknown (pseudo) atomic model $v^* \in A$ for the biomolecule from Cryo-SPA data $y_1, \dots, y_m \in Y$ as in (1.1) with $p_i = x^* = \mathcal{B}(v^*)$, i.e., $y_i := \mathcal{A}(\phi_i \cdot \mathcal{B}(v^*)) + e_i$.

Next, it is often possible to let G act directly on A so that $\phi \cdot \mathcal{B}(v) \approx \mathcal{B}(\phi \cdot v)$ holds for any $\phi \in G$ and $v \in A$. One can then rephrase the above as

$$(1.5) \quad y_i := (\mathcal{A} \circ \mathcal{B})(\phi_i \cdot v^*) + e_i \quad \text{with } \phi_i \in G \text{ unknown.}$$

Heterogeneous particles: The task is to estimate particle specific (pseudo) atomic models $v_1^*, \dots, v_m^* \in A$ that represent different conformations of the biomolecule from Cryo-SPA data $y_1, \dots, y_m \in Y$ as in (1.1) with $p_i = \mathcal{B}(v_i^*)$. The approach we take views these conformations as deformations of a *common* (pseudo) atomic model $v^* \in A$ (template).

If one models deformation in 3D map space as $\mathcal{W}: \mathfrak{X} \times X \rightarrow X$, then the task is to estimate the template $v^* \in A$ along with particle-specific deformation parameters $\psi_1, \dots, \psi_m \in \mathfrak{X}$ from

$$y_i := \mathcal{A}\left(\phi_i \cdot \mathcal{W}(\psi_i, \mathcal{B}(v^*))\right) + e_i \quad \text{with } \phi_i \in G \text{ unknown.}$$

Note here that $p_i := \mathcal{W}(\psi_i, \mathcal{B}(v^*)) \in X$ is the 3D map of the i :th particle.

One of the main reasons for considering joint 3D reconstruction and model building over a sequential approach is that in the former, one can more easily enforce biophysical constraints. To enable this, one has a mapping $\mathcal{V}: \mathfrak{A} \times A \rightarrow A$ that directly defines deformations of (pseudo) atomic models². If we, in addition, define particle-specific poses as actions of G on A , then the task is to estimate the template (pseudo) atomic model $v^* \in A$ along with particle-specific deformation parameters $\vartheta_1, \dots, \vartheta_m \in \mathfrak{A}$ from Cryo-SPA data $y_1, \dots, y_m \in Y$ where

$$(1.6) \quad y_i := \mathcal{A}\left(\mathcal{B}(\phi_i \cdot \mathcal{V}(\vartheta_i, v))\right) + e_i \quad \text{with } \phi_i \in G \text{ unknown.}$$

Then, $v_i := \mathcal{V}(\vartheta_i, v)$ for $i = 1, \dots, m$ are the particle specific (pseudo) atomic models representing the various conformations of the biomolecule.

1.4. Overview of paper and related work. The paper develops methods from shape analysis for estimating a (pseudo) atomic model of a biomolecule from Cryo-SPA particle images (data), i.e., to perform joint 3D map estimation and model building (subsection 1.3.4). The approach is general and applies to many types of (pseudo) atomic models.

The specific setting. To simplify the presentation, we focus on biomolecules that are given as single-chain proteins. Additionally, we assume poses are known and particle images are from the same conformation (homogeneous particles), so joint 3D map estimation and model building corresponds to solving the inverse problem in (1.5) with known poses. Finally, we also disregard side-chain conformations, so our (pseudo) atomic model encodes the backbone conformation.

Structure of paper. As stated above, we apply shape matching to recover the backbone conformation of a protein from Cryo-SPA data of that protein.

The protein is assumed to be in a single conformation, so Cryo-SPA data is from homogeneous particles. Next, the shape space represents possible backbone conformations of the linear sequence of amino acids (primary structure) that makes up the protein. We identify a suitable Lie group that acts on this shape space by folding the backbone in a manner consistent with its possible conformations. Indeed, instead of acting on protein backbones with diffeomorphisms, we ensure proper, rigid transformations of the chains by restricting shape matching to a finite-dimensional matrix Lie group. Thereby, we avoid having to work with the infinite-dimensional Lie group of diffeomorphisms, which simplifies not only the theory but also comes with computational benefits.

Contrary to standard shape matching, however, the template and target shapes in our setting reside in different spaces, which are related to each other via a forward model, as described in the following.

The paper is structured as follows. In section 2 we present a brief an overview of shape matching in a general setting and outline some gradient-based computational approaches for matching. In section 3 we describe a mathematical model for the protein backbone that is required for defining the shape space. We also describe the forward model and perform

²Such a deformation model would be consistent with a deformation of 3D maps, $\mathcal{W}: \mathfrak{X} \times X \rightarrow X$, if for any $\psi \in \mathfrak{X}$, there is a $\vartheta \in \mathfrak{A}$ such that $\mathcal{W}(\psi, \cdot) \circ \mathcal{B} \approx \mathcal{B} \circ \mathcal{V}(\vartheta, \cdot)$.

the computations necessary for shape matching in the specific setting of model building in Cryo-SPA. In particular, [subsection 3.2.2](#) provides explicit expressions for gradients needed in shape matching. [Section 4](#) contains a computational example. More specifically, we apply the framework described in the article to capture closed-to-open dynamics of an adenylate kinase protein. We end the paper with some conclusions and an outlook on possible future research directions in [section 5](#). In particular, we discuss how to extend the shape analysis method to the heterogeneous particle setting. We also mention how to extend the approach to include pose estimation and conformations of side-chains.

Related work. 3D map estimation and model building are in Cryo-SPA commonly performed sequentially. The latter amounts to interpreting an estimated 3D map with atomic models, a task that requires high levels of expertise and labor-intensive manual intervention. This is in Cryo-SPA commonly performed as a separate step applied to the output from 3D map estimation, and many papers deal with how to automate this post-processing step ([subsection 1.3.3](#)).

A different approach that is less explored is to jointly perform 3D reconstruction and model building ([subsection 1.3.4](#)). Here, instead of recovering particle specific 3D maps from Cryo-SPA data, one directly recovers the (pseudo) atomic structures of the particle-specific conformations of the biomolecule. These conformations are given in terms of their (pseudo) atomic structures that are elements in some manifold A .

A natural strategy for joint 3D reconstruction and model building would be to mimic current methods for joint pose and 3D map estimation, namely to set up an iterative refinement scheme that alternates between updating the 3D map and the model. The drawback with such a strategy is the difficulty in accounting for the geometry of the manifold A during reconstruction.

Mathematical theory of shape matching combined with variational regularization offers means for performing reconstruction while accounting for the geometry of A . The overall idea is to view the particles (representing various conformations of the biomolecule) as different deformations of a common template model. This is consistent with the assumption in Cryo-SPA that all particles represent the same biomolecule. Joint 3D reconstruction and model building can then be seen as matching the “shape” of a template against an indirectly observed target (indirect registration). An example of this in the context of tomographic reconstruction is [\[67\]](#). That approach was extended along various directions in [\[21, 20, 46\]](#), see also the survey in [\[48\]](#). The shape matching used in these publications considers shapes of 2D/3D volumetric maps. This paper extends that theory to matching shapes of (pseudo) atomic models. The differential geometric tools necessary for this have close resemblance to those developed in [\[29\]](#) for modelling protein dynamics.

Another differential geometric approach for joint 3D reconstruction and model building is [\[34\]](#). It is based on estimating the torsion and bond angles of the atomic model in each conformation as a linear combination of the eigenfunctions of the Laplace operator in the manifold A of conformations.

We finally mention [\[72\]](#), which is a deep learning-based approach that incorporates model building into the CryoDRGN method [\[97\]](#) for joint pose and 3D map estimation. Hence, the method in [\[72\]](#) jointly performs pose estimation, 3D reconstruction, and model building. However, interpretability remains an issue since the output is a probability density in a la-

latent space (with unknown geometry) and moving around in this latent space corresponds to selecting possible conformations.

2. Shape matching. In general, matching deformable objects refers to the task of aligning selected features of a template object (e.g., landmarks) with corresponding features of a target object. As discussed in [subsection 1.3](#) above, our premise is to use shape matching, largely following the setup described by [\[15\]](#).

The starting point is to consider the set V of deformable shapes (shape space) that we seek to match against each other. V is often a vector space, but this is not a necessity and V is sometimes endowed with a manifold structure.

The deformations used for matching deformable objects in V against each other are given by acting on V with a group G . Stated formally, the group action $\Phi: G \times V \rightarrow V$ represents deformations of elements in V that are parametrized by elements in G . Additionally, in shape matching one also assumes that G has a manifold structure where the group operations of multiplication and inversion are smooth maps, i.e., G is a Lie group with Lie algebra denoted by \mathfrak{g} .

Remark 2.1. *The typical treatment of shape matching considers diffeomorphisms acting on various deformable objects, like point clouds, curves, surfaces, 3D volumes or currents. The Lie group G is here an infinite dimensional subgroup of the group of diffeomorphisms, e.g., one commonly works with Fréchet Lie groups of diffeomorphisms. This results in a rather intricate mathematical theory. In contrast, in our adaptation of shape matching for modelling deformation of protein structures, we only need to consider a finite-dimensional Lie group G .*

2.1. Direct matching. Matching a template $w \in V$ against a target $y \in V$ is in shape matching stated as the task of finding a group element $g \in G$ that parametrizes a deformation $\Phi: G \times V \rightarrow V$ which maps the template as close as possible to the target while minimizing the *matching energy*:

$$(2.1) \quad g \mapsto \mathcal{L}_V(\Phi(g, w), y) + \lambda d_G^2(g, e) \quad \text{for } g \in G,$$

where $e \in G$ is the identity element, $\mathcal{L}_V: V \times V \rightarrow \mathbb{R}$ (*data fidelity* functional) quantifies similarity in V , $d_G: G \times G \rightarrow \mathbb{R}$ is a distance on G , and $\lambda > 0$ determines the amount of regularization.

An issue with solving [\(2.1\)](#) is that the evaluation of the d_G -metric itself involves solving an optimization problem, so the minimizing the functional in [\(2.1\)](#) is a coupled optimization problem over a Lie group. One could consider manifold optimization methods [\[85, 12\]](#), but there is a simpler way. Indeed, the problem solves itself when the distance d_G corresponds to a right invariant Riemannian metric. To see this, note first that the minimization of the functional in [\(2.1\)](#) can be replaced with minimizing a curve $\gamma: [0, 1] \rightarrow G$ in the group

$$(2.2) \quad \gamma \mapsto \mathcal{L}_V(\Phi(\gamma(1), w), y) + \lambda \int_0^1 \langle \dot{\gamma}(t), \dot{\gamma}(t) \rangle_{\gamma(t)} dt \quad \text{such that } \gamma(0) = e,$$

with $\langle \cdot, \cdot \rangle$ denoting a right-invariant metric on G . Next, if γ in [\(2.2\)](#) is sufficiently smooth,

then one can express it as a solution to the flow equation

$$(2.3) \quad \begin{cases} \dot{\gamma}(t) = dR_{\gamma(t)}(\nu(t)) \\ \gamma(0) = e \end{cases} \quad \text{for some } \nu: [0, 1] \rightarrow \mathfrak{g},$$

where $dR_g: \mathfrak{g} \rightarrow T_g G$ is the derivative of the right translation map $R_g: G \rightarrow G$ at the identity, i.e., the map $R_g(h) = hg$. Henceforth, $\gamma^\nu: [0, 1] \rightarrow G$ denotes the curve solving (2.3) for a specific choice of $\nu: [0, 1] \rightarrow \mathfrak{g}$. Note that when G is connected, there exists for any $g \in G$ a curve γ^ν such that $\gamma^\nu(1) = g$. This correspondence between curves in G and \mathfrak{g} allows us to rephrase the minimization of (2.2) over curves in the Lie group G as a minimization over curves $\nu: [0, 1] \rightarrow \mathfrak{g}$ in the Lie algebra $\mathfrak{g} = T_e G$ (which has a vector space structure):

$$(2.4) \quad \nu \mapsto \mathcal{L}_V\left(\Phi(\gamma^\nu(1), w), y\right) + \lambda \int_0^1 \langle \dot{\gamma}^\nu(t), \dot{\gamma}^\nu(t) \rangle_{\gamma^\nu(t)} dt.$$

The metric $\langle \cdot, \cdot \rangle$ can be constructed by specifying an inner product (\cdot, \cdot) on \mathfrak{g} . The metric at the remaining points of G is then given by translating the inner product from the right. We here consider inner products on \mathfrak{g} of the form

$$(u, u) := \langle \mathbb{I}u, u \rangle_{\mathfrak{g}^*, \mathfrak{g}} \quad \text{for } u \in \mathfrak{g}$$

where $\mathbb{I}: \mathfrak{g} \rightarrow \mathfrak{g}^*$ is a symmetric positive semi-definite operator and $\langle \cdot, \cdot \rangle_{\mathfrak{g}^*, \mathfrak{g}}$ denotes duality pairing between the algebra and its dual. By right invariance of the metric, we have

$$\int_0^1 \langle \dot{\gamma}^\nu(t), \dot{\gamma}^\nu(t) \rangle_{\gamma^\nu(t)} dt = \int_0^1 \langle \nu(t), \nu(t) \rangle_e dt.$$

Hence, the energy functional we seek to minimize during matching reads as

$$(2.5) \quad \mathcal{E}(\nu) := \mathcal{L}_V\left(\Phi(\gamma^\nu(1), w), y\right) + \lambda \mathcal{S}(\nu)$$

where $\lambda > 0$ and $\mathcal{S}(\nu) \in \mathbb{R}$ is the regularization term given by

$$(2.6) \quad \mathcal{S}(\nu) := \int_0^1 \langle \nu(t), \nu(t) \rangle_e dt$$

The choice of $\lambda > 0$ in (2.5) balances the regularization in (2.6), which penalizes deformations that vary strongly, against the need to match the target as quantified by the \mathcal{L}_V -term (data fidelity) in (2.5).

2.2. Indirect matching. In direct matching, the task is to match a deformable object $w \in V$ (template) against another deformable object $y \in V$ (target). Indirect matching considers the more general setting where the target and template reside in different spaces. This is typically the case in an inverse problem setting, where the target is given by (noisy) indirect observations.

Stated formally, in indirect matching, one assumes that observations of the target reside in a set Y (*data space*) that is different from V . Next, we have an operator (*forward model*)

$$(2.7) \quad \mathcal{F}: V \rightarrow Y$$

that models how a deformable object in V generates a noise-free observation in data space Y . The task in indirect matching is to match a template $w \in V$ against data $y \in Y$ that represents a noisy indirect observation of the unknown target $y \in V$.

One can formalize this task in a way that is completely analogous to (2.5) for direct matching, but here one needs to account for the forward model in (2.7). Then, indirect matching is the task of finding a curve $\nu: [0, 1] \rightarrow \mathfrak{g}$ that maps w as close as possible to y while minimizing the following modified *matching energy* between $w \in V$ and $y \in Y$:

$$(2.8) \quad \mathcal{E}(\nu) := \mathcal{L}_Y((\mathcal{F} \circ \Phi)(\gamma^\nu(1), w), y) + \lambda \mathcal{S}(\nu) \quad \text{for a curve } \nu: [0, 1] \rightarrow \mathfrak{g}.$$

The difference to (2.5) is that the data fidelity $\mathcal{L}_Y: Y \times Y \rightarrow \mathbb{R}$ quantifies similarity in data space Y . A common approach is to choose it as an appropriate affine transformation of the neg-log of the data likelihood, so minimizing only the \mathcal{L}_Y -term corresponds to maximum likelihood estimation.

2.3. Approaches for minimization. The task of minimizing the functional in (2.8) over curves $\nu: [0, 1] \rightarrow \mathfrak{g}$ can be reduced to a dynamical formulation. To see this, note first that the data fidelity depends on only $\gamma^\nu(1) \in G$, i.e., on the *final* time point of the curve $t \mapsto \gamma^\nu(t)$. Hence, an optimal curve $t \mapsto \nu(t)$ must follow the dynamics determined by the action functional consisting only of the regularization term of (2.8) defined in (2.6), i.e.,

$$(2.9) \quad \mathcal{S}(\nu) := \int_0^1 \langle m(t), \nu(t) \rangle_{\mathfrak{g}^*, \mathfrak{g}} dt$$

where $m: [0, 1] \rightarrow \mathfrak{g}^*$ (*momentum*) is the dual of $\nu: [0, 1] \rightarrow \mathfrak{g}$. Due to the right-invariance of the metric, standard methods in geometric mechanics [60, Theorem 13.5.3] yield that $t \mapsto m(t)$ evolves according to the *Euler–Arnold equation*:

$$(2.10) \quad \dot{m}(t) = \text{ad}_\nu^*(m(t)) \quad \text{for } t \in [0, 1].$$

Here, $\text{ad}_\nu^*: \mathfrak{g}^* \rightarrow \mathfrak{g}^*$ is defined implicitly by the requirement that the mapping

$$\mathfrak{g} \times \mathfrak{g}^* \ni (\nu(t), m(t)) \mapsto \text{ad}_\nu^*(m(t)) \in \mathfrak{g}^*$$

is for any $t \in [0, 1]$ the adjoint of the Lie bracket on \mathfrak{g} with respect to the inner product. Thus, performance for approaches that perform matching by minimizing an energy of the form (2.8) depends highly on the choice of inner product. In addition, the group G must be known to completely deduce an explicit expression for the mapping ad_ν^* .

We next consider two algorithms for computing a minimizer, the shooting method and the path method.

2.3.1. Shooting method. The shooting method arises from the Euler–Arnold equations (2.10). The idea is to start with an initial guess of the initial value of the momentum, and then to integrate (2.10) to obtain the full curve $m: [0, 1] \rightarrow \mathfrak{g}^*$. From this curve, one then obtains the curve $\nu: [0, 1] \rightarrow \mathfrak{g}$, which in turn can be used to compute the group element in G acting on the template.

Note that the regularization energy is conserved along the dynamics of the Euler–Arnold equations (2.10). Indeed, it holds that

$$\begin{aligned} \frac{d}{dt} \langle m(t), \nu(t) \rangle_{\mathfrak{g}^*, \mathfrak{g}} &= 2 \langle \dot{m}(t), \nu(t) \rangle_{\mathfrak{g}^*, \mathfrak{g}} = 2 \langle \text{ad}_\nu^*(m(t)), \nu(t) \rangle_{\mathfrak{g}^*, \mathfrak{g}} \\ &= 2 \langle m(t), \text{ad}_\nu(\nu(t)) \rangle_{\mathfrak{g}^*, \mathfrak{g}} = 0. \end{aligned}$$

Therefore, one only considers the regularization term at the initial momentum,

$$\tilde{\mathcal{S}}(m(0)) = \langle m(0), \nu(0) \rangle_{\mathfrak{g}^*, \mathfrak{g}}$$

and the optimization only needs to be over possible *initial* momenta to obtain the optimal deformation.

The above approach is called the shooting method, since one guesses an initial momentum that is then “shot away” to obtain the deformation of the template. One then evaluates the quality of the match by computing the matching energy and then “re-aims” to improve the matching, i.e., update the momentum by taking a step with a scheme given by an optimization method, like gradient descent, Broyden–Fletcher–Goldfarb–Shanno (BFGS)-type method or a conjugate gradient type of method. The shooting method is summarized in [Algorithm 2.1](#).

Algorithm 2.1 Shooting method for shape matching

- **Initialize:** Suitable guess for initial momentum $m_0^{[0]}$, optimization routine, numerical integration parameters
 - **While** m_0 changes OR fixed number of steps **do**:
 - Numerically integrate the Euler–Arnold equation (2.10) to obtain $\nu: [0, 1] \rightarrow \mathfrak{g}$
 - Numerically integrate (2.3) to obtain an approximation of $\gamma^\nu(1)$
 - Evaluate $\mathcal{L}_V(\Phi(\gamma^\nu(1), w), y) + \lambda \tilde{\mathcal{S}}(m_0(0))$
 - Compute $m^{[j+1]}$ by taking a step with the optimization routine
 - **If needed:**
 - * Compute $\nabla_{\nu_0^{[j]}} \mathcal{L}_V(\Phi(\gamma^\nu(1), w), y)$ using [Theorem 2.2](#)
-

2.3.2. Path method. The path method is an alternative to the shooting method that avoids solving the Euler–Arnold equation in (2.10).

Given a partition of the time interval, $0 = t_0 < t_1 < \dots < t_n = 1$, we optimize the values of the momentum at those points, m_{t_0}, \dots, m_{t_n} . The method is summarized in [Algorithm 2.2](#)

Algorithm 2.2 Path method for shape matching

- **Initialize:** Time points t_0, \dots, t_n , suitable guesses for momentum path $m_0^{[0]}, m_1^{[0]}, \dots, m_n^{[0]}$, optimization routine, numerical integration parameters
 - **While** m_0, \dots, m_n changes **OR** fixed number of steps **do**:
 - Numerically integrate (2.3) using m_0, \dots, m_n to approximate $\gamma^\nu(1)$
 - Evaluate $\mathcal{L}_V(\Phi(\gamma^\nu(1), w), y) + \lambda \mathcal{S}(\nu)$
 - **For** $k = 0, \dots, m$ **do**:
 - * Set $m_{t_k}^{[j+1]}$ by taking a step with the optimization routine
 - * **If needed**:
 - Compute $\nabla_{\nu_{t_k}^{[j]}} \mathcal{E}$ with Theorem 2.2
-

2.3.3. Gradient of the objective. Algorithms 2.1 and 2.2 requires computing the gradient of \mathcal{E} in (2.8) with respect to the curve $\nu: [0, 1] \rightarrow \mathfrak{g}$.

In the case when G is a matrix Lie group, the gradient is straightforward to compute compared to the case of the diffeomorphism group, since there are no spatial derivatives to account for. Next, for matrix Lie groups, the group operation is just given by matrix multiplication. Furthermore, for fixed $g \in G$, the tangent left translation $dL_g: \mathfrak{g} \rightarrow T_g(G)$ and tangent right translation $dR_g: \mathfrak{g} \rightarrow T_g(G)$ are also given by matrix multiplications:

$$dL_g(u) = gu \quad \text{and} \quad dR_g(u) = ug \quad \text{for a matrix } u \in \mathfrak{g}.$$

Theorem 2.2 explicitly computes the gradient of the energy $\mathcal{E}: \mathcal{C}^\infty([0, 1], \mathfrak{g}) \rightarrow \mathbb{R}$ in (2.8) for matching $w \in V$ against $y \in Y$ in this specific setting. The statement holds for general Lie groups G acting on shape spaces V and a simplified proof for the case when G is a matrix Lie group is given in Appendix A.

Theorem 2.2. *Let the space V of deformable objects (shape space) be a manifold and the space Y of data (data space) is a Hilbert space. Next, let $w \in V$ and $y \in Y$ and assume that elements in V are deformed by acting with a Lie group G on V through an action $\Phi: G \times V \rightarrow V$. Furthermore, define $\mathcal{E}: \mathcal{C}^\infty([0, 1], \mathfrak{g}) \rightarrow \mathbb{R}$ following (2.8), as*

$$(2.11) \quad \mathcal{E}(\nu) := \lambda \mathcal{S}(\nu) + \mathcal{L}_Y\left((\mathcal{F} \circ \Phi)(\gamma^\nu(1), w), y\right) \quad \text{for a curve } \nu: [0, 1] \rightarrow \mathfrak{g},$$

where $\gamma^\nu: [0, 1] \rightarrow G$ is given by solving (2.3), $\mathcal{S}: \mathcal{C}^\infty([0, 1], \mathfrak{g}) \rightarrow \mathbb{R}$ is as in (2.9), and $\mathcal{F}: V \rightarrow Y$ is assumed to be differentiable. When G is a matrix Lie group and $\mathcal{L}_Y: Y \times Y \rightarrow \mathbb{R}$ (data fidelity) above is given by the squared Y -norm as

$$\mathcal{L}_Y(y, \tilde{y}) := \frac{1}{2} \|y - \tilde{y}\|_Y^2 \quad \text{for } y, \tilde{y} \in Y,$$

then the gradient of \mathcal{E} at $\nu: [0, 1] \rightarrow \mathfrak{g}$ is given by

$$(2.12) \quad \nabla \mathcal{E}(\nu)(t) = \lambda \nu(t) + (\text{Ad}_{(\gamma^\nu)^{-1}})^* \left(\left(d(\mathcal{F} \circ \Phi)(\cdot, w) \circ L_{\gamma^\nu(1)}(e) \right)^* (r_{w,y}) \right),$$

where $r_{w,y} \in Y$ is a residual term that is defined as

$$(2.13) \quad r_{w,y} := \left((\mathcal{F} \circ \Phi)(\gamma^\nu(1), w) - y \right).$$

Remark 2.3. To interpret the terms/factors in (2.12), note that the first term is the gradient of the regularization term. The second term is the gradient of the data fidelity term and is a composition of several expressions. The residual term $r_{w,y}$ is the difference between the deformed template transformed with \mathcal{F} into data space and the target, see (2.13). To the residual, we apply several adjoint mappings. These appear in various ways. $\mathcal{F} \circ \Phi(\cdot, w)$ arises from the application of the forward model and the deformation of the template. Further, $L_{\gamma^\nu(1)}$ and $\text{Ad}_{(\gamma^\nu)^{-1}}$ appears when computing the first order variation of $\gamma^\nu(t)$, which is a crucial step in the proof of Theorem 2.2.

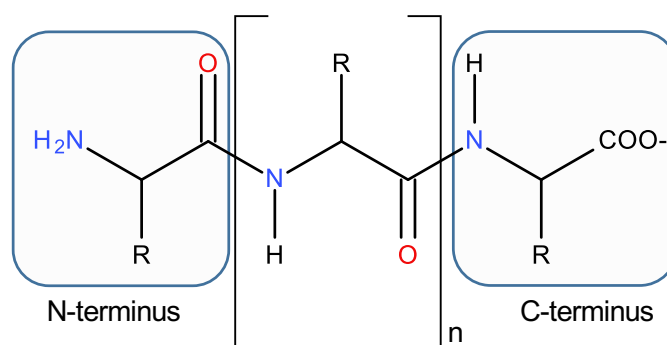
While Theorem 2.2 provides all the ingredients for computing the gradient, an explicit expression is only obtainable when one specifies the manifold V of deformable objects. One also needs to specify a Lie group G whose action $\Phi: G \times V \rightarrow V$ on V represents deformations. The metric on G , which is specified by \mathbb{I} , is next used to penalize “unnatural” deformations. Finally, we have the set Y (data space) whose elements represent data, which are noisy indirect observations of deformable objects, and the forward model $\mathcal{F}: V \rightarrow Y$ models the data in Y that is generated by a deformable object in V .

3. Joint reconstruction and model building in Cryo-SPA (revision in progress). As shown in subsection 1.3.4, one can view the problem of recovering the backbone conformation of a protein from Cryo-SPA data as indirect matching. This matching problem is, in turn, a special case of shape matching that is outlined in section 2 with specific choices of shape space, group action, and data fidelity functional. Before specifying these, we start with a brief overview of how protein structure is described.

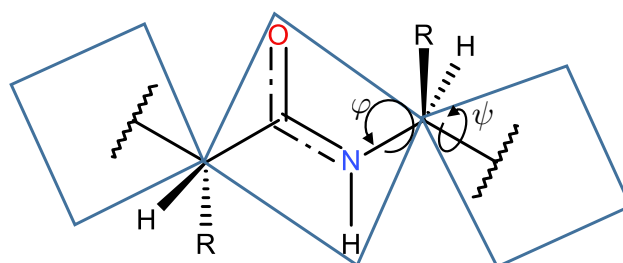
3.1. Protein structures. Proteins are large biomolecules that are made up of polypeptides, each consisting of many (typically 100–300) residues. In a polypeptide, there is a backbone chain consisting of repeating nitrogen-carbon-carbon units. Residues are small molecules (about 0.5 nm in ‘diameter’) that consist of a backbone part, formed by nine atoms $\text{H}_2\text{N}-\text{CH}-\text{C}_\alpha-\text{O}_2\text{H}$, and a side chain (R-group), which is an amino acid that is covalently bonded to the central carbon atom (denoted by C_α) in the backbone. The backbone part of a residue are the same for all proteins, whereas the side chains vary. For most (not all) proteins, there are 20 possible amino acids that can serve as side chains, i.e., there are 20 possible residues. Figure 1a gives a schematic representation of the structure, together with the first and last polypeptide unit, known as the N-terminus and C-terminus, respectively. In Figure 1b, we further see the orientations of the side chain and substituents.

There are several ways to describe the structure of a protein. First is its *primary structure*, which is an ordered list of the residues that make up the polymer chain(s). Mathematically, this is a labelled linear graph (or string) that has the peptide bonds as edges and the types of residue side chains (there are 20 possibilities) as labels. The primary structure can nowadays be easily determined from the gene sequence that codes for the protein.

Next is *secondary structures* that focus on describing the basic folding patterns that the backbone typically displays. These patterns are divided into two groups: α -helices and β -



(a) Schematic of a polypeptide backbone consisting of n repeating units of $N-C_{\alpha}-C(\text{carbonyl})$. In general, the nitrogen has a hydrogen substituent. The first carbon (not shown) is known as the α -carbon, and it has a hydrogen substituent and a substituent called the side chain (residue) denoted by the letter R . The second carbon (carbonyl carbon) is double bonded to an oxygen atom.



(b) Schematic of the 3D orientation of the peptide units. Each section of the polypeptide between two C_{α} each are co-planar, whereas the hydrogen atoms (H) and side chains (R) extend forward or backward out from the plane.

Figure 1: The “anatomy” of the backbone of a protein.

sheets. An α -helix refers to a coiling of the backbone that is held together by H-bonding between the backbone residues. The resulting helical structure typically contains about ten amino acids (three turns) but some may have over forty residues. A β -sheet is the case when the backbone is arranged along several parallel or antiparallel (with respect to the $H_2N \rightarrow \dots \rightarrow CO_2H$ direction of the backbone chain) strands that form a pleated (often twisted) sheet-like structure. These strands are typically 5–10 amino acids long, and they are connected laterally by H-bonds. As outlined in [47], both these patterns are mathematically associated with an Z -symmetry of the protein backbone, and where the combinatorial structure defined by β -sheets is much richer than what comes from α -helices.

Finally, we have the *tertiary structure* that is the full description of the 3D arrangement of atoms and (covalent) bonds that make up the protein. It is determined by the spatial folding of the backbone (backbone conformation) along with the conformations of the peptide-units

(side-chains). It also includes specifying the rather flexible loops that join the fairly rigid “rod”-like structures formed by α -helices and “plates” formed by β -sheets³.

As already noted, the backbone is made up in the same way for all natural proteins, but the types and locations of the side chains differ across proteins. The identities of these side chains influence the secondary and tertiary structures [3, Chapter 3]. In fact, it is commonly accepted by scientists that all information required to specify the tertiary structure of a protein is contained in its primary structure. To actually infer/reconstruct the tertiary structure from the primary structure is known as (ab initio) folding. AlphaFold 2 [56] used deep learning to “address” this challenge for single chain proteins, and it was later extended to multichain proteins in [35]. Recently, the release of AlphaFold 3 [1] showed how deep diffusion-based models can be used to predict joint structure of complexes including proteins, nucleic acids, small molecules, ions and modified residues. However, recovering intrinsic dynamics of isolated (single chain) proteins is still an open problem.

3.2. Shape space for protein structures. Constructing a shape space for a class of biomolecules corresponds to a mathematical formalization of their relevant structural patterns. Focus here is on the backbone conformation of proteins that consist of a single polypeptide⁴.

An important requirement on the shape space in our setting is that it should be possible to map an element in the shape space to a 3D map (electrostatic potential) generated by the protein structure encoded by the shape space element. This indicates that it should be enough to represent the structure as a labelled point cloud, where the labelling is given by the atomic nuclei. However, when handling protein dynamics, it is highly desirable to exclude deformations that are not biophysical. This becomes easier if the shape space encodes more of the chemical information, like information about some of the chemical bonds. In fact, dynamics of biomolecules, and proteins in particular, tends to preserve the covalent bonds. Similarly, local hydrogen bonds that make up secondary structures are also often preserved. Hence, the (intrinsic) dynamics of isolated biomolecules is to a large extent governed by the formation and destruction of distant hydrogen bonds.

The primary structure for a protein that consists of N residues can be represented as an array, (r_1, \dots, r_N) where each residue r_i can have 20 possible labels (determined by the 20 possible amino acids that a side-chain can be). Next, the four atoms in the section of the backbone between two C_α atoms are co-planar (see Figure 1b), so the conformation of the backbone can be described with two dihedral angles for each residue. This means the conformation of the backbone can be described as an array in $SO(3)^N$. In addition, one needs four dihedral angles to encode the conformation of a side-chain in a residue [33, 11, 88], so side-chain conformations can be described as an array in $(SO(3)^2)^N$. Hence, an all-atom-model applicable to most proteins with primary structure (r_1, \dots, r_N) is given as an element in $(SO(3) \times SO(3)^2)^N$.

3.2.1. Protein backbone conformations. The 3D spatial arrangement (structure) of the backbone for a fixed protein is determined by the 3D positions of the C_α atoms in its backbone. If A is the set of possible 3D arrangements of the backbone, then its elements are merely arrays

³One still lacks a comprehensive formal mathematical language for describing flexible loops [47].

⁴Most proteins consist of a single polypeptide, but some can consist of several polypeptides, like hemoglobin that is composed of four polypeptides.

of the form $a = (a_1, \dots, a_N) \in \mathbb{R}^{3 \times N}$ where N is the number of residues and each $a_i \in \mathbb{R}^3$ represents the position of the i :th C_α atom. From such a representation, one can compute the electrostatic potential generated by the C_α atoms in the backbone. With an additional small effort, can also include the contributions to the electrostatic potential from the entire backbone (but disregarding the side chains). This is represented by a mapping $\mathcal{B}: A \rightarrow X$ and it may be a sufficiently good approximation of the 3D map for the entire protein. The latter is important when one needs to simulate 2D TEM images generated by the protein structure.

Elements in A do not explicitly encode the covalent bonds in the protein backbone. These are important since biophysically feasible deformations of the backbone tend to preserve them. One can implicitly account for these covalent bonds without introducing a computationally demanding graph-type data structure to handle. The idea is to consider inter-atomic distances between the C_α atoms in the backbone. These distances are given as

$$\delta_j := \|a_{j+1} - a_j\| \in \mathbb{R}_+ \quad \text{for all } j = 1, \dots, N-1,$$

and allowable backbone deformations are now those that ensure $\delta_j = \delta > 0$ for all j . This assumption that interatomic distances are preserved opens up for representing the backbone structure via the relative positions of the C_α atoms. To define the shape space, first consider all relative positions of the C_α atoms in the backbone, which is an array in $\mathbb{R}^{3 \times (N-1)}$:

$$(a_2 - a_1, \dots, a_N - a_{N-1}) \in \mathbb{R}^{3 \times (N-1)} \quad \text{with } (a_1, a_2, \dots, a_N) \in A.$$

This could be our shape space, but we also seek a bijection between the shape space and A . Therefore, we supplement the above relative positions with the absolute position of the first C_α atom, i.e., our shape space V consists of N -arrays of the form

$$v = (a_1, a_2 - a_1, \dots, a_N - a_{N-1}) \in \mathbb{R}^{3 \times N} \quad \text{with } (a_1, a_2, \dots, a_N) \in A.$$

As indicated, the two different representations of the backbone structure in A and V are related via the bijective map $\mathcal{M}: V \rightarrow A$ that is defined as

$$\mathcal{M}(v) := \left(v_1, v_1 + v_2, v_1 + v_2 + v_3, \dots, \sum_{j=1}^N v_j \right)$$

with inverse $\mathcal{M}^{-1}: A \rightarrow V$ given by

$$\mathcal{M}^{-1}(a) = (a_1, a_2 - a_1, \dots, a_N - a_{N-1}).$$

We next define the Lie group action that deforms the backbone structure of a protein. Let $v, v' \in V$ be two different backbone structures of the protein. Since these have the same interatomic distances, there exist rotation matrices $\rho_1, \dots, \rho_N \in \text{SO}(3)$ such that $v'_i = \rho_i v_i$. The deformation of the backbone of the protein can then be represented by acting with the Lie group $G := (\text{SO}(3))^N$ on V via component-wise matrix-vector multiplication:

$$\Phi: G \times V \rightarrow V \quad \text{where } \Phi(g, v) := (\rho_1 v_1, \dots, \rho_N v_N) \quad \text{with } g = (\rho_1, \dots, \rho_N) \in G.$$

This means acting with $(\text{SO}(3))^N$ on the relative atom positions for the C_α atoms in the backbone, which in particular preserves interatomic distances. Note also that one cannot independently move a single C_α atom in the backbone, e.g., moving the first one will affect the entire backbone.

Remark 3.1. *An all-atom model for the protein is given by its primary structure, an element in A (backbone conformation) or V , and conformations of the N residues.*

Remark 3.2. *There is a subtle difference between the notion of conformation and structure. The conformation is the spatial 3D arrangement of the protein up to the pose of the protein, whereas structure refers to the actual position in space (which also includes its pose). For biological interpretation, it is enough to work with conformation, but for simulating TEM images one also needs the structure since the simulation depends on the pose.*

3.2.2. The Cryo-EM forward operator. The primary structure of the protein is known, and it is used to define the shape space V of possible backbone structures for the protein. These are only indirectly observable by TEM imaging. The *forward operator* models how a deformable object in V (see [subsection 3.2.1](#)) gives rise to an observable 2D TEM image.

2D TEM images can be seen as digitized functions in $Y := \mathcal{L}^2(\mathbb{R}^2)$. We now describe the forward operator used for generating an element $y_i \in Y$ from a backbone structure $v_i \in V$ for $i = 1, \dots, m$. The idea is to first map v_i to the corresponding 3D point cloud representation in A via $\mathcal{M}: V \rightarrow A$. Next, we create a (approximate) 3D map that serves as input for an operator that models TEM image formation. One way to do this is to replace each atom in the backbone with a 3D Gaussian, a step that is mathematically formalized by the operator $\mathcal{B}: A \rightarrow X$ where $X = \mathcal{L}^2(\mathbb{R}^3)$ is the vector space of 3D maps, i.e., functions on \mathbb{R}^3 that can be the electrostatic potential for a protein embedded in vitrified aqueous buffer. Finally, we generate a 2D TEM image from the (approximate) 3D map by an operator $\mathcal{P}: X \rightarrow Y$ that models TEM image formation. The simplest such model is given by the parallel beam ray transform that disregards the TEM optics and detector response. The forward operator $\mathcal{F}: V \rightarrow Y$ is now given as (see also [Figure 2](#))

$$(3.1) \quad \mathcal{F} := \mathcal{P} \circ \mathcal{B} \circ \mathcal{M}.$$

When \mathcal{P} is the parallel beam ray transform, then one can evaluate [\(3.1\)](#) in a computationally feasible manner as follows: Perform a geometric projection of the input 3D point cloud along the TEM optical axis onto the 2D TEM detector plane. Then, apply the 2D analogue of \mathcal{B} to the 2D point cloud. This short-cut also works when the TEM image formation model \mathcal{P} incorporates the effects of the TEM optics.

3.3. Shape matching of protein backbones. We here describe how the general theory for shape matching in [section 2](#) can be adapted to the setting in [subsections 3.2.1](#) and [3.2.2](#), i.e., to register a template backbone in $V := \mathbb{R}^{3 \times N}$ for a protein by a group action in $G := (\text{SO}(3))^N$ against a target backbone that is indirectly observed as a 2D TEM image in $Y := \mathcal{L}^2(\mathbb{R}^2)$. [Subsection 3.2.1](#) offers a motivation for these choices, and solving this indirect registration task will be based on minimizing the energy functional in [\(2.11\)](#). Hence, a key topic is to express the gradient in [\(2.12\)](#) in this specific setting.

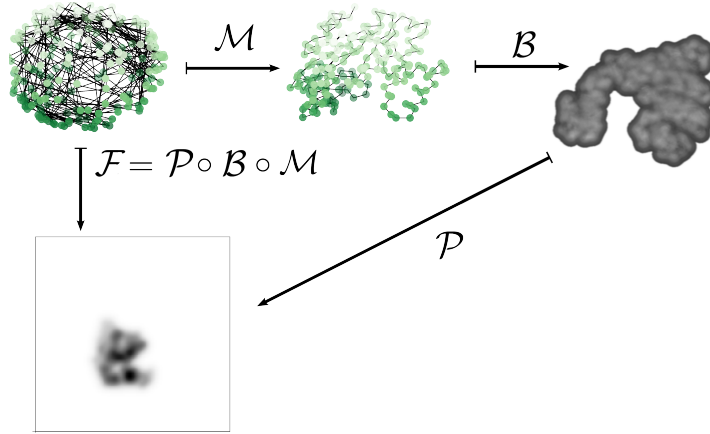


Figure 2: The forward model is built up from three intermediate steps. First is to use \mathcal{M} to map V (relative positions) to corresponding absolute atomic positions, i.e., elements in A . Next, we use \mathcal{B} to generate a (approximate) 3D map in X , which is then mapped by \mathcal{P} to a 2D TEM image in Y .

Note first that the Lie algebra \mathfrak{g} of the Lie group G consists of the direct sum of N copies of $\mathfrak{so}(3)$, which is the Lie algebra of skew-symmetric matrices. The mapping $\Phi: G \times V \rightarrow V$ that represents the action of the group G on V is here given by component-wise matrix-vector multiplication. Further, we set $\mathbb{I} = (\mathbb{I}_1, \dots, \mathbb{I}_N)$, where each \mathbb{I}_i maps a $u_i \in \mathfrak{so}(3)$ to its momentum, and let $\mathbb{I}u = (\mathbb{I}_1 u_1, \dots, \mathbb{I}_N u_N)$. To construct the inner product on the Lie algebra $\mathfrak{g} = (\mathfrak{so}(3))^N$, we first consider the Frobenius inner product on $\mathfrak{so}(3)$ given by $\langle \tilde{u}, u \rangle_F = -\text{tr}(\tilde{u}u)$. Any invertible self adjoint positive map relative to the Frobenius inner product induces an inner product on $\mathfrak{so}(3)$: $\langle \tilde{u}, u \rangle = \langle \mathbb{I}\tilde{u}, u \rangle_F$, so we take the inner product on $\mathfrak{g} = (\mathfrak{so}(3))^N$ to be

$$\langle \tilde{u}, u \rangle = - \sum_{i=1}^N \text{tr}(u_i \mathbb{I}_i \tilde{u}_i)$$

The forward operator $\mathcal{F}: V \rightarrow Y$ in (3.1) can, as described in subsection 3.3, be computed more efficiently as follows: Use $\mathcal{M}(v) = a$ to map the relative positions of the backbone C_α atoms $v \in V$ to the corresponding 3D cloud of atomic positions $a \in A$. Then, geometrically project the atomic positions along the TEM optical axis down to the 2D detector plane: $\pi: A \rightarrow \mathbb{R}^{2 \times N}$ where the i :th component is given by

$$(\pi(a))_i = (1 \ 0 \ 0) \cdot a_i + (0 \ 1 \ 0) \cdot a_i \quad \text{for } i = 1, \dots, N.$$

Note that any projection onto a plane can be viewed as a projection onto the (x, y) -plane in the right coordinates. Therefore, by transforming coordinates, using the above projection and its adjoint, and transforming back into the original coordinates, all projections, and their adjoints can be obtained. Finally, the projected atomic positions are mapped into $\mathcal{L}^2(\mathbb{R}^2)$

by $\mathcal{B}_{2D}: \mathbb{R}^{2 \times N} \rightarrow Y$, that sends a 2D point cloud $p \in \mathbb{R}^{2 \times N}$ to a linear combination of 2D Gaussians

$$\mathcal{B}_{2D}(p)(\cdot) = \sum_{i=1}^N s_i (\tau_{p_i} \circ \varphi_{\sigma_i})(\cdot),$$

where s_1, \dots, s_N are weights describing the relative importance of each atom and $\sigma_1, \dots, \sigma_N$ are parameters determining the width of the Gaussians. These parameters depend on the atom represented by the point p_i in the point cloud, with φ_{σ_i} denoting the function

$$\varphi_{\sigma_i}(x, y) := \frac{1}{2\pi\sigma_i^2} \exp\left(-\frac{x^2 + y^2}{2\sigma_i^2}\right)$$

and $\tau_{p_i}: Y \rightarrow Y$ denoting translation by the point p_i . The forward operator in (3.1) can then be expressed as

$$\mathcal{F} = \mathcal{B}_{2D} \circ \pi \circ \mathcal{M}.$$

Consider now the energy functional $\mathcal{E}: \mathcal{C}^\infty([0, 1], \mathfrak{g}) \rightarrow \mathbb{R}$ in (2.11). Corollary B.1 in Appendix B computes its gradient by applying Theorem 2.2 to this setting. This yields a closed-form expression for the gradient of $\mathcal{E}(\nu)$ that is useful in performing joint 3D reconstruction and model building (subsection 1.3.4).

Remark 3.3. *In subsection 3.3 we have assumed that the particle is in a single poses. It is possible to include more poses into this framework with minimal changes. Indeed, to have two poses, one takes two projection functions $\pi_1: A \rightarrow \mathbb{R}^{2 \times N}$ and $\pi_2: A \rightarrow \mathbb{R}^{2 \times N}$ and proceeds to work with two forward models,*

$$\mathcal{F}_1 = \mathcal{B}_{2D} \circ \pi_1 \circ \mathcal{M} \quad \text{and} \quad \mathcal{F}_2 = \mathcal{B}_{2D} \circ \pi_2 \circ \mathcal{M}.$$

One then sets $\tilde{Y} = Y \oplus Y$ and takes the target data to be (y_1, y_2) so the data fidelity is

$$(y_1, y_2) \mapsto \frac{1}{2} \left(\left\| \mathcal{F}_1(\Phi_{\gamma_{\nu(1)}}(a_0)) - y_1 \right\|_{\mathcal{L}^2}^2 + \left\| \mathcal{F}_2(\Phi_{\gamma_{\nu(1)}}(a_0)) - y_2 \right\|_{\mathcal{L}^2}^2 \right).$$

The gradient of this modified functional is computed by taking the sum of the gradients given by Corollary B.1 applied to each term. The extension to an arbitrary number of poses is straightforward.

4. Numerical experiment on adenylate kinase. We now apply our method for indirect matching of 3D protein backbone structures. The focus of this paper is to introduce shape matching to the setting of protein data. Therefore, we perform illustrative proof-of-concept computations, which are deliberately kept simple.⁵

The protein considered in this numerical experiment is an adenylate kinase protein, which is chosen as it has a clear closed-to-open transition. Intuitively, this means that the protein initially has a “closed lid” that gradually opens, see Figure 3 for an illustration of 3D arrangement of the open and closed backbone conformation.

⁵All results presented in this section are produced using code available at <https://github.com/erik-grennberg-jansson/protein-lddmm>.

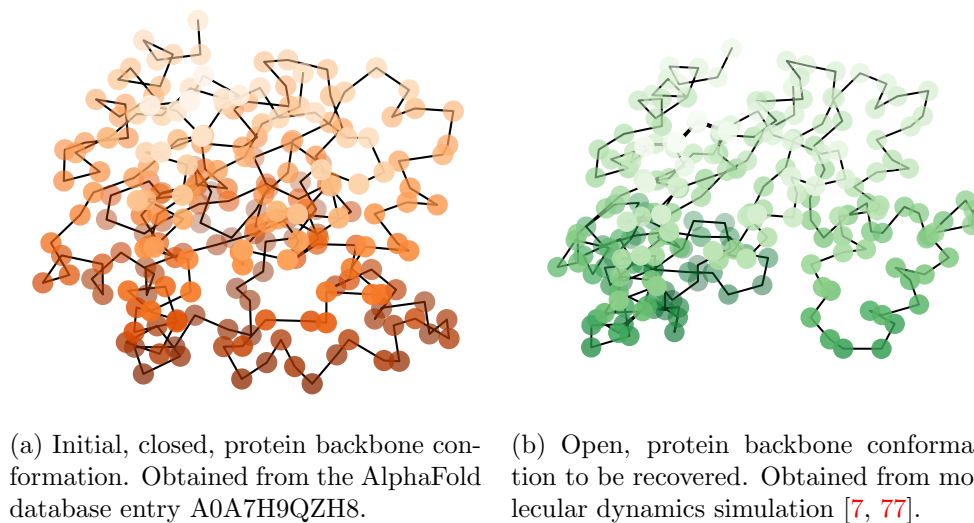


Figure 3: The initial and final conformation of the C_α atoms in the backbone of the closed-to-open adenylate kinase deformation. Note that this depicts the 3D arrangements, i.e., elements in A .

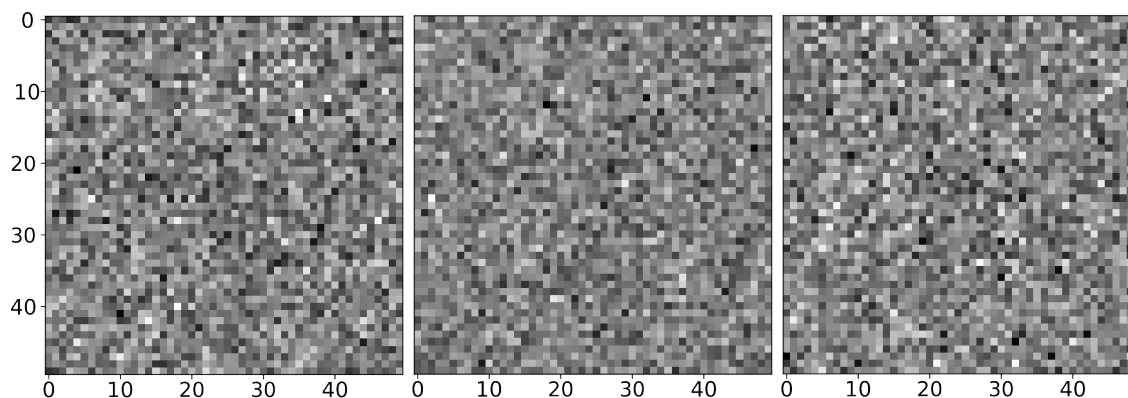


Figure 4: The data (in Y) used to deform the template. The three images are obtained by applying the forward model to the protein conformation in Figure 3b and adding Gaussian noise with standard deviation 1.0 to each pixel.

To construct the target, we apply the forward model to the final frame of a protein trajectory from [7, 77], which was obtained by molecular dynamics simulations.

To construct the template, we use data from the AlphaFold database corresponding to

the closed conformation⁶ [56, 90]. As AlphaFold data is not necessarily aligned with the molecular dynamics trajectory, we use Procrustes analysis to rotate and mirror the AlphaFold point cloud to align with the first frame of the protein trajectory. Briefly, Procrustes analysis computes the orthogonal linear transformation aligning one point cloud with another that is optimal in the sense that it minimizes the *Procrustes distance*. For details, see [43, 57]. In future work, we aim to estimate the alignment of the AlphaFold data from the observed images. This would entail solving yet another inverse problem. Techniques to achieve this goal could be achieved by extending the method introduced in [30].

We only consider the C_α atoms in the protein backbone. We aim to reconstruct the structure in the final frame of the trajectory based off indirect observations of it, as described in subsection 3.3. It is not a priori clear which, and how many, projections should be selected. Note that in the absence of noise, three projections: on the (x, y) plane, the (x, z) plane, and the (y, z) plane capture all information about the protein. Therefore, a naive first approach is to proceed as in Remark 3.3, but this time with three elements in Y instead of two.

When we apply \mathcal{B}_{2D} to the projected point clouds, we use a width (standard deviation) of 2.0. The images are in practice discretized as pixel images with resolution 50×50 pixels. We then add, to each pixel in the images, Gaussian observational noise with standard deviation 1.0 and thereby obtain the data in Figure 4. With this choice of observational noise, the signal-to-noise ratio, computed by dividing the variance of the pixel image without noise with the noise variance, is on average, 0.003, or expressed in decibels, -25.181 dB.

To compute the matching, we use the path discretization method of Algorithm 2.2 so that the curve of algebra elements $\nu: [0, 1] \rightarrow (\mathfrak{so}(3))^N$ is discretized at fixed time grid points $t_n = n\delta t$ where $\delta t = 0.01$ and $n = 0, 1, 2, \dots, 100$. Further, we make a non-informed choice of the momentum mapping and set \mathbb{I} to be the identity.

As described in subsection 3.3, we must compute the deformation of the template by determining the path of group elements $\rho_0, \rho_{\delta t}, \dots, \rho_1$ determined by $\nu_0, \nu_{\delta t}, \dots, \nu_1$. This is done by applying the Lie–Euler integrator with a step size of $\delta t = 0.01$ to the flow equation $\dot{\rho} = \rho\nu$, where ρ_0 is initialized as the identity element of $(\text{SO}(3))^N$. Applying this integrator guarantees that ρ_1 is an element of $(\text{SO}(3))^N$ [54]. Finally, we compute the gradient of \mathcal{E} with respect to ν_t , denoted by $\nabla_{\nu_t}\mathcal{E}$ as outlined in subsection 3.3. We then optimize \mathcal{E} by using the L-BFGS-B algorithm implemented in the Python scientific computing package SciPy, [92]. This algorithm is a limited-memory version of the BFGS algorithm, see [16] for details. To obtain a suitable initial guess for the optimizer, we run 50 steps of gradient descent, with a step size of 10^{-5} .

Figure 5 illustrate $\mathcal{F}_1, \mathcal{F}_2$ and \mathcal{F}_3 applied to the non-deformed template shown in Figure 3a, $\mathcal{F}_1, \mathcal{F}_2$ and \mathcal{F}_3 applied to the deformed template, the directly observed noisy target images as well as $\mathcal{F}_1, \mathcal{F}_2$ and \mathcal{F}_3 applied to the non-directly observed target shown in Figure 3b. All of these images are in Y . It is clear that we manage to capture the closed-to-open movement of the protein, at least along the directions of the projections.

Consider now the reconstructed 3D protein conformation in Figure 7a, i.e., the reconstruction depicted in the set A of possible 3D arrangements of the backbone.

It is obvious that this is a poor reconstruction of the target conformation. However, the

⁶<https://alphafold.ebi.ac.uk/entry/A0A7H9QZH8>

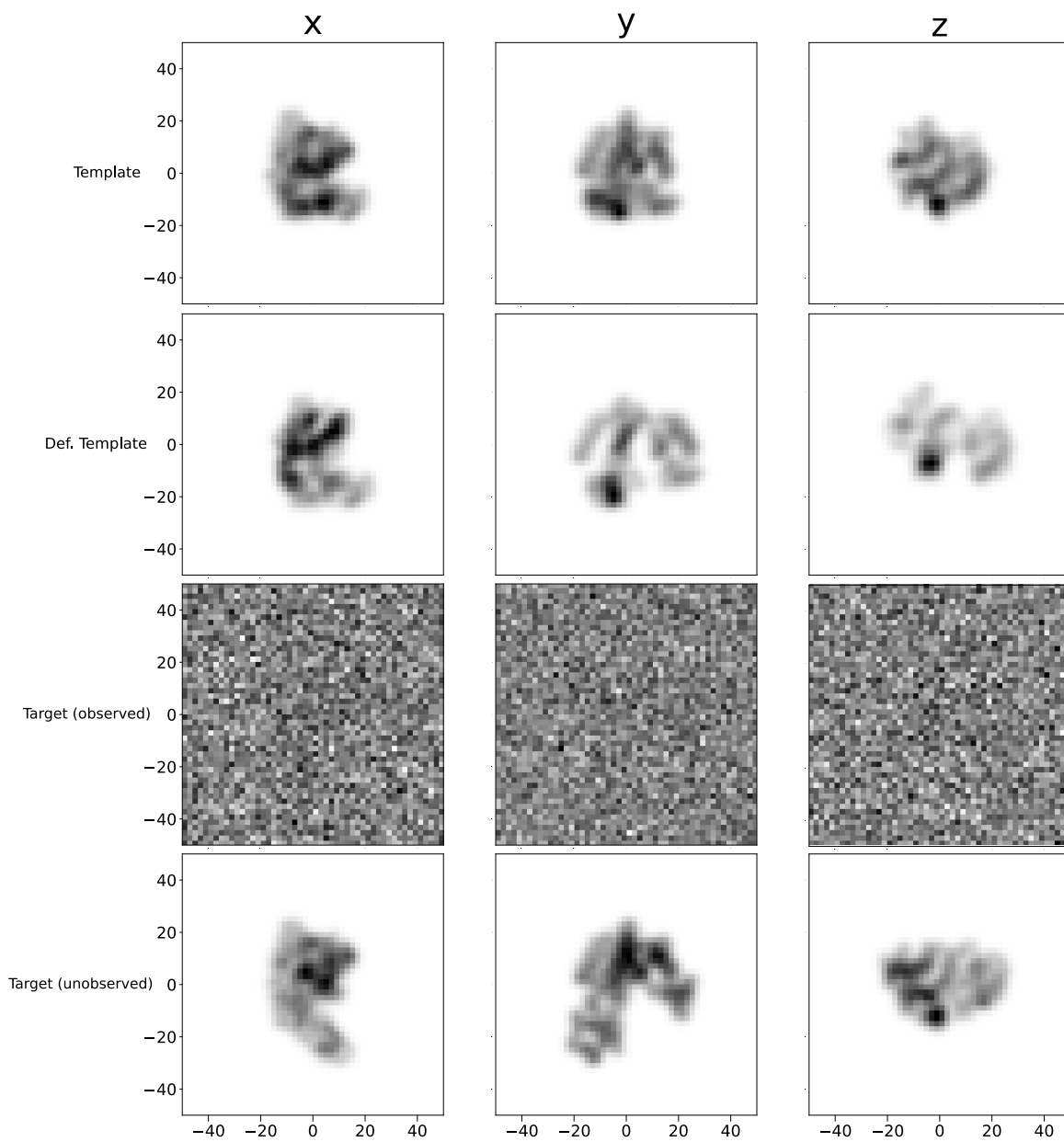


Figure 5: The results of applying the indirect shape matching algorithm to the template (Figure 3a) using projections along the x , y and z axes. Note that while not perfect, the deformation along these axes decently captures the changes between the initial and target conformation.

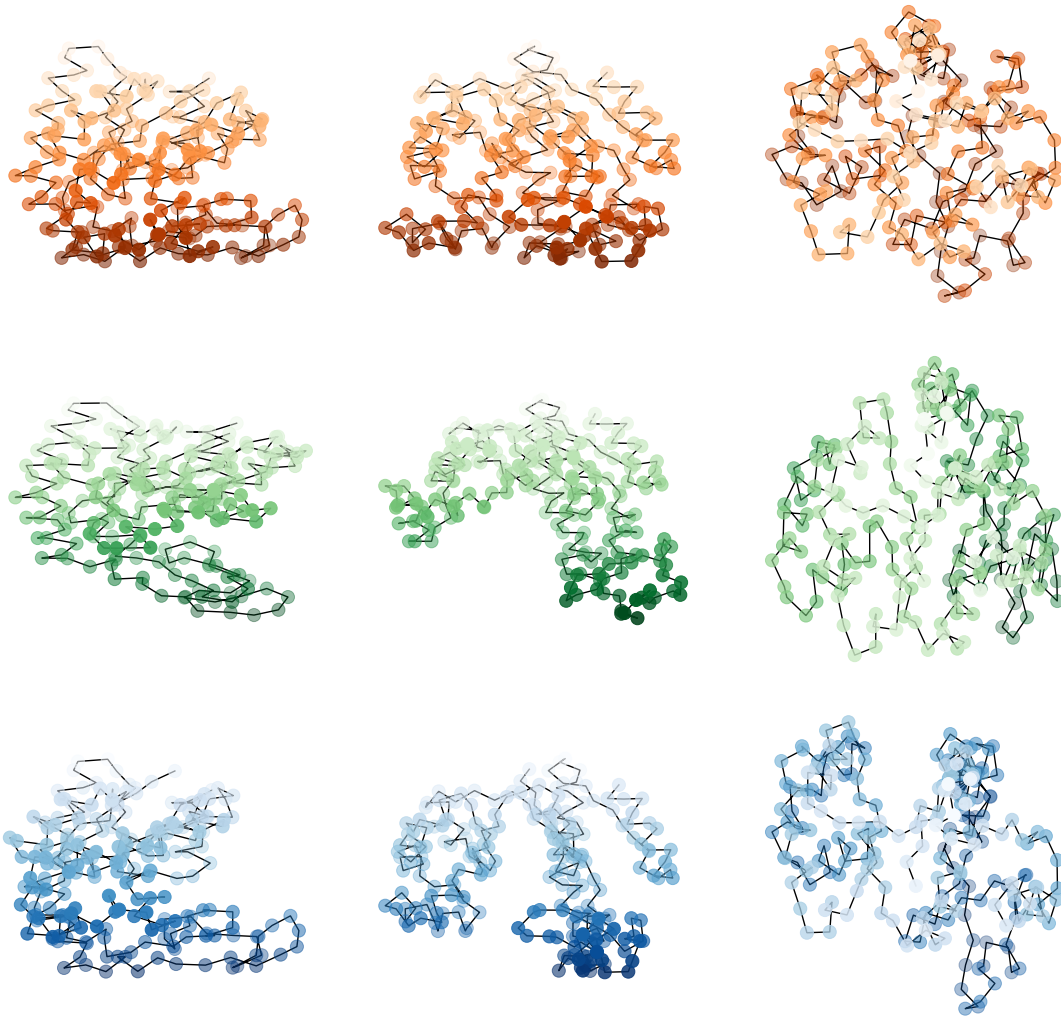


Figure 6: The reconstructed 3D arrangement (blue) together with the template (orange) and non-directly observed target (green), viewed along the same three projection angles as in Figure 5. Rows depict template, target and deformed template respectively. Note that we generally capture the deformation, especially the large closed-to-open movement in the $x - z$ plane (middle column).

key takeaway is that we manage to capture the deformation in the directions we project, see Figure 6, in which the reconstruction is depicted in the 3D arrangement, i.e., as an element in A .

To improve the reconstruction, we increase the number of projection images to 300. Again, we proceed as in Remark 3.3, but this time with 300 elements in Y instead of two. The random projections are selected by uniformly randomly sampling 300 rotation matrices. These matrices each describe a change to coordinates in which the projection is computed as the

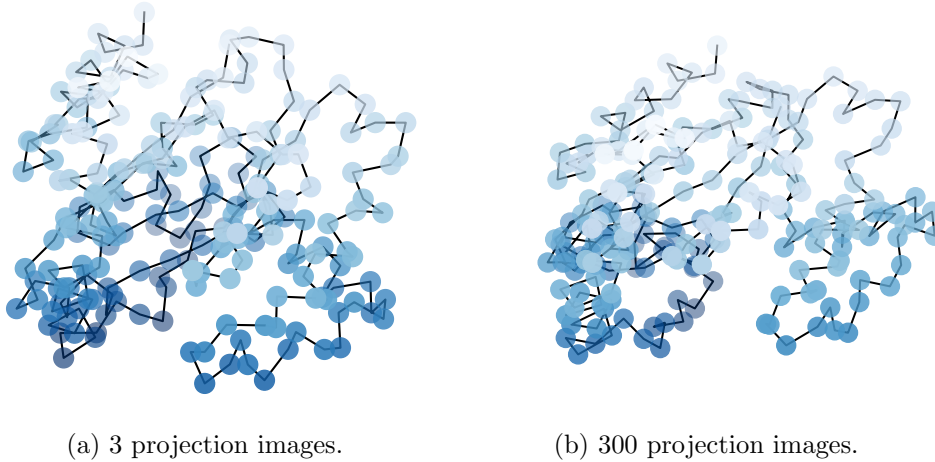


Figure 7: Two reconstructions of the target conformation using a different number of projections. Note that this depicts the 3D spatial arrangements, i.e. elements in A . By comparing with [Figure 3b](#), it is clear that the number of projections improves the reconstruction.

projection on the $x - y$ plane.

Keeping everything else as above, we recover the reconstruction in [Figure 7b](#). In [Figure 8](#) we illustrate the deformation path of the 3D arrangements of the template, i.e., the deformation path in A . Comparing the deformed template to the target conformation in [Figure 3b](#), it is clear that this is a better reconstruction. We manage to capture the closed-to-open movement of the adylenate protein and decently compute a reconstruction of the final structure. The matching is by no means perfect, but the large-scale movement is indeed captured and highlights that shape matching can be used for this purpose.

To give a quantitative assessment of the dependence of the quality of the reconstruction on the number of projections, we use Procrustes analysis to compare the deformed point cloud to the reconstructed conformation. Procrustes analysis aligns points clouds by minimizing the *Procrustes score*, which is a statistical measure of shape similarity. A lower score means that two compared point clouds are more similar [\[43, 57\]](#). We run, for $k = 2^1, 2^2, \dots, 2^9$ randomly chosen projections, the reconstruction procedure as described above, using an image noise standard deviation of 1.0.

To give an idea of the uncertainty of the reconstruction, we repeat the procedure, with new noisy targets, 20 times for each noise level. Then, the 20 reconstructions are assessed against the ground truth, i.e., the target point cloud, by computing the average Procrustes score. This results in [Figure 9](#), where the average Procrustes score is plotted against the number of projections in a log-log scale, together with the 90% quantiles. [Figure 9](#) confirms that indeed, more projections results in a lower Procrustes score. This indicates that the reconstructed protein conformation is closer to the target conformation in the sense of point clouds if more projections are used. [Figure 9](#) indicates that the Procrustes score decreases as

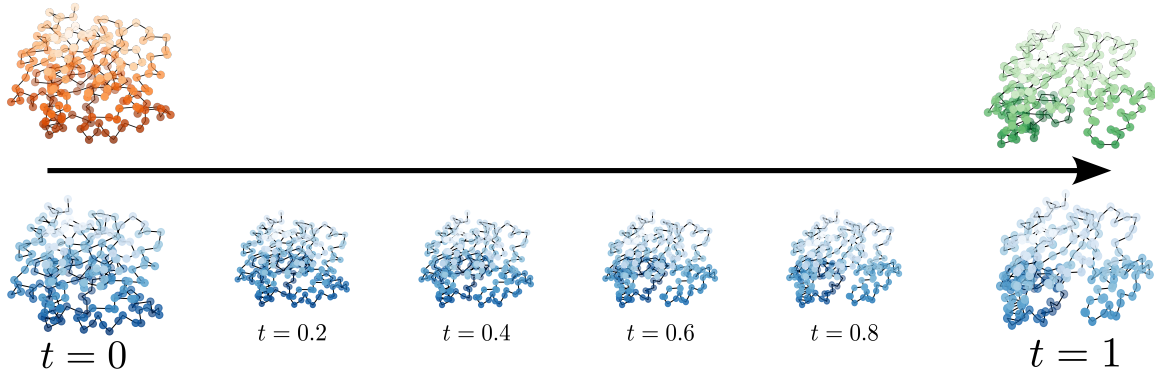


Figure 8: The results of applying the indirect shape matching algorithm to the template (orange structure). The evolution is shown at each included time grid point (blue structures). Compare with the final, not directly observed, frame (green structure).

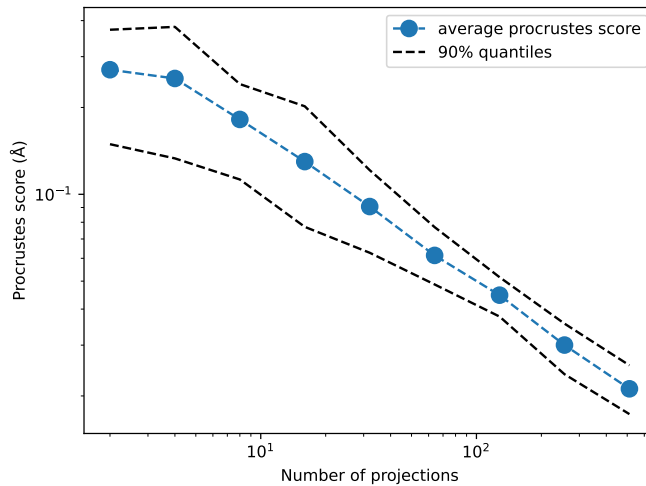


Figure 9: The average Procrustes score, in Ångströms, is plotted against the number of projections in a log-log scale. Note that the more projections that are used, the lower the Procrustes score.

$\mathcal{O}(N_P^r)$, where N_P is the number of projections. A linear regression fit estimates the slope r as -0.48 , indicating that $r \approx 0.5$.

Moreover, the uncertainty becomes smaller as the number of projections goes up. This translates in practice to the fact that if we just have a few randomly chosen projections, we need to be lucky and obtain good projection angles, whereas if we have more, we can be more certain that we have enough projection angles to obtain a good reconstruction.

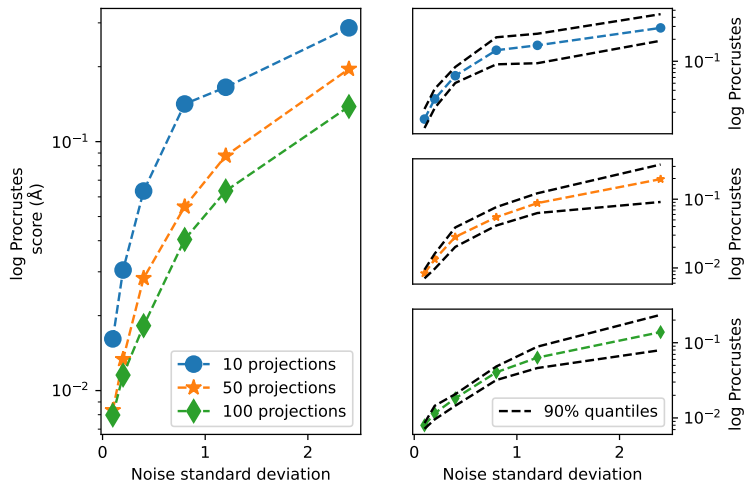


Figure 10: The average Procrustes score, in Ångströms, is plotted against the number of projections in a log-lin scale. Note that the robustness against noise increases with increasing number of projections. Further, the number of projections seems to influence the width of the quantiles, indicating that the uncertainty of the reconstruction is dependent on the number of projections as well as on the noise level.

We perform a similar experiment to investigate the effect of the noise. For a fixed number of projections, we run the reconstruction algorithm as above, but with varying image noise standard deviations. For 10, 50 and 100 projections, we let the noise standard deviations take the values 0.1, 0.2, 0.4, 0.8, 1.2 and 2.4, repeating the reconstruction $M = 20$ times. The 20 reconstructions are assessed against the ground truth by computing the Procrustes scores. This results in Figure 10, where the average Procrustes score is plotted against the number of projections in a log-log scale, together with the 90% quantiles. We observe that, as expected, more projections increase the reconstruction performance for higher noise standard deviations, but that the decrease in performance is qualitatively similar for 10, 50 and 100 projections. The number of projections further seems to influence how the width of the quantiles increases as the variance of the image noise increases, more projection images results in less wide quantiles, indicating that the uncertainty of the reconstruction is dependent on the number of projections as well as on the noise level.

There are other ways than Procrustes analysis to quantitatively assess the reconstruction, see for instance [86]. We intend to investigate the use of other protein similarity measures in future work.

5. Conclusions and outlook. In this work, we have demonstrated that geodesic shape matching can play a role in the reconstruction of 3D backbone conformations from noisy Cryo-SPA data. We achieved this by modelling the conformations of a backbone as deformations of a template given by the action of a finite-dimensional group on a suitable set of deformable

options. The group in this case is the N -fold direct product of $\text{SO}(3)$.

We have presented two gradient-based algorithms to compute the matching and have illustrated the method in a computational example encompassing not only a qualitative assessment of the reconstruction, but also quantitative aspects using Procrustes analysis to assess the reconstruction's sensitivity to the number of projections used and to the image noise level.

The above approach can be extended in several directions, all motivated by applications in Cryo-SPA. A straightforward extension is to combine the method presented in this paper with, for instance, existing pose estimation algorithms, like [31], to improve the viability of this method on real world-data.

Furthermore, the shape matching framework is very flexible. In principle, with all else fixed, the geometric behavior of the method is only affected by the choice of regularization term. This opens two directions of future research. Firstly, the regularization term is fixed up to the choice of the operator \mathbb{I} . As an example, the i :th component of \mathbb{I} models the inertia of the i :th C_α atom. Hence, one can in principle account for the influence of side chains, since a long, heavy side chain means that the protein rotates more easily in certain directions. Likewise, \mathbb{I} could also account for internal forces in the protein that are generated by electrical and chemical interactions.

Secondly, the framework is not qualitatively affected by the data fidelity term in (2.8). This means that it is possible to include potentials that allow us to take the effect of bindings and nonlinear interactions between atoms in the protein into account. A third possible improvement is to incorporate an optimal-transport based similarity measure, that would allow for increased robustness to image noise.

Another direction of future research is to forgo the geodesic shape matching framework altogether, and instead work with gradient flows directly on the space of protein backbones chains using an adaptation of the method described in [6]. This type of method should result in a substantial complexity reduction.

Appendix A. Proof of Theorem 2.2. We here prove [Theorem 2.2](#) in the case when G is a matrix Lie group. The proof is an adaptation of the proof of [\[8, Theorem 2.1\]](#). Hence, we start with the following finite-dimensional variant of [\[8, Lemma 2.1\]](#) that computes the variation of the $\gamma^\nu: [0, 1] \rightarrow G$ where γ^ν solves the flow equation [\(2.3\)](#) under the perturbation of the curve $\nu: [0, 1] \rightarrow \mathfrak{g}$.

Lemma A.1. *Let ν be a smooth curve in the Lie algebra \mathfrak{g} of the matrix Lie group G and let $\gamma^\nu: [0, 1] \rightarrow G$ denote the curve that solves the flow equation $\dot{\gamma}^\nu = \nu(t)\gamma^\nu(t)$, $\gamma^\nu(0) = e$. The (infinitesimal) variation of the G -curve γ^ν , denoted by $\delta_\eta\gamma$, as the \mathfrak{g} -curve ν is perturbed with $\eta \in \mathcal{L}^2([0, 1], \mathfrak{g})$ is then given by*

$$(A.1) \quad \delta_\eta\gamma^\nu(t) = dL_{\gamma^\nu(t)} \left(\int_0^t \text{Ad}_{(\gamma^\nu(s))^{-1}}(\eta(s)) ds \right)$$

where the adjoint representation $\text{Ad}_g: \mathfrak{g} \rightarrow \mathfrak{g}$ for fixed $g \in G$ is given by $\text{Ad}_g(u) := gug^{-1}$.

Proof. G is a matrix Lie group, so the curve $\gamma^\nu: [0, 1] \rightarrow G$ with $\nu \in \mathcal{L}^2([0, 1], \mathfrak{g})$ given by in [\(2.3\)](#) takes the form

$$\dot{\gamma}^\nu(t) = \nu(t)\gamma(t), \quad \gamma(0) = I \in G.$$

Let us take an admissible first order variation of ν in the η -direction, which is fixed, by considering

$$\nu_\epsilon(t) := \nu(t) + \epsilon\eta(t).$$

This variation induces a variation in γ^ν along the η -direction that can be expressed as

$$(A.2) \quad \dot{\gamma}^{\nu_\epsilon}(t) = (\nu(t) + \epsilon\eta(t))\gamma^{\nu_\epsilon}(t).$$

Furthermore, we also get that the infinitesimal variation in γ^ν along the η -direction is given by

$$(A.3) \quad \delta_\eta\gamma^\nu(t) = \left. \frac{d}{d\epsilon} \gamma^{\nu_\epsilon}(t) \right|_{\epsilon=0}.$$

Differentiate [\(A.2\)](#) with respect to ϵ and evaluate it at $\epsilon = 0$. Combining this with [\(A.3\)](#) yields the following differential equation:

$$(A.4) \quad \partial_t \delta_\eta\gamma^\nu(t) = \nu(t)\delta_\eta\gamma^\nu(t) + \eta(t)\gamma^\nu(t).$$

The variation of $\gamma^\nu(t)$ along the η -direction is thus given by a solution of [\(A.4\)](#), which in turn can be expressed as

$$(A.5) \quad \delta_\eta\gamma^\nu(t) = \gamma^\nu(t) \int_0^t (\gamma^\nu(s))^{-1} \eta(s) \gamma(s) ds.$$

Indeed, differentiating [\(A.5\)](#) with respect to t yields [\(A.4\)](#). To complete the proof, we next insert the definition of the adjoint representation. This gives us

$$(\gamma^\nu(s))^{-1} \eta(s) \gamma^\nu(s) = \text{Ad}_{(\gamma^\nu(s))^{-1}}(\eta(s)).$$

Finally, we note that,

$$\int_0^t (\gamma^\nu(s))^{-1} \eta(s) \gamma^\nu(s) ds \in \mathfrak{g} \quad \text{for any } t \in [0, 1],$$

so

$$\delta_\eta \gamma^\nu(t) = \gamma^\nu(t) \int_0^t (\gamma^\nu(s))^{-1} \eta(s) \gamma^\nu(s) ds = dL_{\gamma(t)} \left(\int_0^t \text{Ad}_{(\gamma^\nu(s))^{-1}}(\eta(s)) ds \right).$$

This completes the proof. \blacksquare

Proof of Theorem 2.2. The Gâteaux derivative of $\mathcal{E}: \mathcal{C}^\infty([0, 1], \mathfrak{g}) \rightarrow \mathbb{R}$ (matching energy) in (2.8) in the direction $\eta \in \mathcal{L}^2([0, 1], \mathfrak{g})$ is defined as

$$(A.6) \quad \delta_\eta \mathcal{E}(\nu) := \lim_{\varepsilon \rightarrow 0} \frac{\mathcal{E}(\nu + \varepsilon \eta) - \mathcal{E}(\nu)}{\varepsilon}.$$

If we define $r_{w,y} \in Y$ as in (2.13), then we can re-write (A.6) as

$$\delta_\eta \mathcal{E}(\nu) = \int_0^1 \langle \nu(t), \eta(t) \rangle_{\mathfrak{g}} dt + \left\langle r_{w,y}, d(\mathcal{F} \circ \Phi(\cdot, w))_{\gamma^\nu(1)}(\delta_\eta \gamma^\nu(1)) \right\rangle_Y.$$

The proof is now completed by using Lemma A.1 to rewrite the second term in the above expression. To see this, note first that

$$\begin{aligned} & \left\langle r_{w,y}, d(\mathcal{F} \circ \Phi(\cdot, w))_{\gamma^\nu(1)}(\delta_\eta \gamma^\nu(1)) \right\rangle_Y \\ &= \left\langle r_{w,y}, d(\mathcal{F} \circ \Phi(\cdot, w))_{\gamma^\nu(1)} d(L_{\gamma^\nu(1)})_e \left(\int_0^1 \text{Ad}_{(\gamma^\nu(t))^{-1}}(\eta(t)) dt \right) \right\rangle_Y \\ &= \left\langle r_{w,y}, \varpi \left(\int_0^1 \text{Ad}_{(\gamma^\nu(t))^{-1}}(\eta(t)) dt \right) \right\rangle_Y = \left\langle \varpi^*(r_{w,y}), \int_0^1 \text{Ad}_{(\gamma^\nu(t))^{-1}}(\eta(t)) dt \right\rangle_Y \end{aligned}$$

where $\varpi: \mathfrak{g} \rightarrow Y$ is the linear mapping

$$\varpi := d(\mathcal{F} \circ \Phi(\cdot, w) \circ L_{\gamma^\nu(1)})_e.$$

The final step is to exchange the order with which we take the t -integral and the Y -inner product:

$$\begin{aligned} \left\langle r_{w,y}, d(\mathcal{F} \circ \Phi(\cdot, w))_{\gamma^\nu(1)}(\delta_\eta \gamma^\nu(1)) \right\rangle_Y &= \left\langle \varpi^*(r_{w,y}), \int_0^1 \text{Ad}_{(\gamma^\nu(t))^{-1}} \eta(t) dt \right\rangle_Y \\ &= \int_0^1 \left\langle \varpi^*(r_{w,y}), \text{Ad}_{(\gamma^\nu(t))^{-1}}(\eta(t)) \right\rangle_{\mathfrak{g}} dt \\ &= \int_0^1 \left\langle (\text{Ad}_{(\gamma^\nu(t))^{-1}})^*(\varpi^*(r_{w,y})), \eta(t) \right\rangle_{\mathfrak{g}} dt. \quad \blacksquare \end{aligned}$$

Appendix B. Gradient calculations. Here, we detail the results of applying the setting of subsection 3.3 to Theorem 2.2 to obtain a closed-form expression for the gradients used in computing the matching in section 4.

Corollary B.1. *Consider the Lie group $G = (\text{SO}(3))^N$ that acts on deformable objects in the shape space $V = \mathbb{R}^{3 \times N}$. Moreover, assume observed data resides in $Y = \mathcal{L}^2(\mathbb{R}^2)$. Next, consider the functional $\mathcal{E}: \mathcal{C}^\infty([0, 1], \mathfrak{g}) \rightarrow \mathbb{R}$ defined as in (2.8) where $\mathfrak{g} = (\mathfrak{so}(3))^N$ is the Lie algebra to G . The target in Y is denoted by y and the template in V by w . Then, the gradient of \mathcal{E} is given as*

$$(B.1) \quad \nabla_\nu \mathcal{E}(\nu) = \lambda \nu + \text{Ad}_{(\gamma^\nu)^{-1}}^* d(\Phi(\cdot, w) \circ L_{\gamma^\nu(t)})_e^* \mathcal{M}^* \pi^* (d\mathcal{B}_{2D})_q^* \eta$$

where

$$\eta = \mathcal{B}_{2D} \circ \pi \circ \mathcal{M}(\Phi(\gamma^\nu(1), w)) - y \quad \text{and} \quad q = \pi \circ \mathcal{M}(\Phi(\gamma^\nu(1), w))$$

and the map

$$y \mapsto \text{Ad}_{(\gamma^\nu(t))^{-1}}^* d(\Phi(\cdot, w) \circ L_{\gamma^\nu(t)})_e^* \mathcal{M}^* \pi^* (d(\mathcal{B}_{2D})_q)^*(y)$$

is computed by the following operators:

1. $((d\mathcal{B}_{2D})_q)^*: Y \rightarrow \mathbb{R}^{2 \times N}$ that is defined as

$$(d(\mathcal{B}_{2D})_q)^*(y) = (s_1(y * \nabla g_{\sigma_1})(q_1), \dots, s_N(y * \nabla g_{\sigma_N})(q_N)) = p \in \mathbb{R}^{2 \times N},$$

2. $\pi^*: \mathbb{R}^{2 \times N} \rightarrow A$ that is defined as

$$\pi^* p = (\Lambda p_1, \Lambda p_2, \dots, \Lambda p_N) = a \in A \quad \text{where} \quad \Lambda = \begin{pmatrix} 1 & 0 \\ 0 & 1 \\ 0 & 0 \end{pmatrix},$$

3. $\mathcal{M}^*: A \rightarrow V$ that is defined as

$$\mathcal{M}^* a = \left(\sum_{i=1}^N a_i \quad \dots \quad a_{N-1} + a_N \quad a_N \right) = v \in V,$$

4. $(d(\Phi(\cdot, w) \circ L_{\gamma^\nu(t)})_e)^*: V \rightarrow \mathfrak{g}$ that is defined as

$$(d(\Phi(\cdot, w) \circ L_{\gamma^\nu(t)})_e)^* v = (-\mathbb{I}_1^{-1} \Pi(w_1 v_1^\top (\gamma^\nu(t))_1) \quad \dots \quad -\mathbb{I}_N^{-1} \Pi(w_N v_N^\top (\gamma^\nu(t))_N)) = u \in \mathfrak{g},$$

where $\Pi: \mathfrak{gl}(3, \mathbb{R}) \rightarrow \mathfrak{so}(3)$ denotes the orthogonal projection relative to the Frobenius inner product onto the Lie algebra $\mathfrak{so}(3)$. Explicitly, $\Pi(W) = (W - W^\top)/2$ for any matrix $W \in \mathfrak{gl}(3, \mathbb{R})$.

5. $\text{Ad}_{\gamma^\nu(t)}^*: \mathfrak{g} \rightarrow \mathfrak{g}$, that is defined as

$$\text{Ad}_{\gamma^\nu(t)}^* u = (\mathbb{I}_1^{-1} \text{Ad}_{(\gamma^\nu(t))_1}^\top \mathbb{I}_1 u_1, \dots, \mathbb{I}_N^{-1} \text{Ad}_{(\gamma^\nu(t))_N}^\top \mathbb{I}_N u_N),$$

for all $u \in \mathfrak{g}$.

Proof. The proof amounts to computing the expressions of the adjoint mappings, which we compute one by one. We first calculate the adjoint of the map $\text{Ad}_\rho: (\mathfrak{so}(3))^N \rightarrow (\mathfrak{so}(3))^N$ for any given $\rho \in (\text{SO}(3))^N$.

Since the map Ad_ρ acts componentwise, we assume for the moment in our calculations that $N = 1$. It holds that

$$(B.2) \quad \langle \text{Ad}_\rho \tilde{u}, u \rangle = \langle \text{Ad}_\rho \tilde{u}, \mathbb{I}u \rangle_F = -\text{tr}(\rho \tilde{u} \rho^\top \mathbb{I}u) = -\text{tr}(\tilde{u} \rho^\top \mathbb{I}u \rho) = \langle \tilde{u}, \text{Ad}_{\rho^\top} \mathbb{I}u \rangle_F,$$

for an arbitrary $u \in \mathfrak{so}(3)$, showing that

$$(B.3) \quad \text{Ad}_\rho^* u = \mathbb{I}^{-1} \text{Ad}_{\rho^\top} \mathbb{I}u.$$

In the general case $N \geq 1$, the formula is given by

$$(B.4) \quad \text{Ad}_\rho^* u = (\mathbb{I}_1^{-1} \text{Ad}_{\rho_1^\top} \mathbb{I}_1 u_1, \dots, \mathbb{I}_N^{-1} \text{Ad}_{\rho_N^\top} \mathbb{I}_N u_N),$$

where $u \in \mathfrak{g}$ is arbitrary.

Next, we calculate the adjoint of the map $d(\Phi(\cdot, v) \circ L_\rho)_e : \mathfrak{g} \rightarrow V$ for a fixed $v \in V$ and $\rho \in G$. Just as when we calculated the adjoint of the adjoint representation, we first restrict ourselves to the case $N = 1$. Differentiating the relation $(\Phi(\cdot, v) \circ L_\rho)(T) = \rho T v$ with respect to an arbitrary $T \in \text{SO}(3)$ gives $d(\Phi(\cdot, v) \circ L_\rho)_e u = \rho u v$, where u is an element of the Lie algebra $\mathfrak{so}(3)$. For an arbitrary vector $b \in \mathbb{R}^3$, we have that

$$(B.5) \quad \begin{aligned} \langle d(\Phi(\cdot, v) \circ L_\rho)_e u, b \rangle &= \langle \rho u v, b \rangle = b^\top \rho u v = \text{tr}(b^\top \rho u v) \\ &= \text{tr}(v b^\top \rho u) = \text{tr}(\Pi(v b^\top \rho) u) = -\left\langle \Pi(v b^\top \rho), u \right\rangle_F, \end{aligned}$$

which shows that

$$(B.6) \quad (d(\Phi(\cdot, v) \circ L_\rho)_e)^* b = -\mathbb{I}^{-1} \Pi(v b^\top \rho),$$

and in the general case for $N \geq 1$ this becomes

$$(d(\Phi(\cdot, v) \circ L_\rho)_e)^* b = (-\mathbb{I}_1^{-1} \Pi(v_1 b_1^\top \rho_1), \dots, -\mathbb{I}_N^{-1} \Pi(v_N b_N^\top \rho_N)).$$

We turn our attention to the adjoints of the forward model. Firstly, the adjoint of the map $\mathcal{M} : V \rightarrow A$ is obtained from the relations

$$\begin{aligned} \langle \mathcal{M} v, a \rangle &= \sum_{i=1}^N \left\langle \sum_{j=1}^i v_j, a_i \right\rangle = \sum_{i=1}^N \sum_{j=1}^i \langle v_j, a_i \rangle \\ &= \sum_{j=1}^N \sum_{i=j}^N \langle v_j, a_i \rangle = \sum_{j=1}^N \left\langle v_j, \sum_{i=j}^N a_i \right\rangle, \end{aligned}$$

showing that

$$(B.7) \quad \mathcal{M}^* a = \left(\sum_{i=1}^N a_i, \dots, a_{N-1} + a_N, a_N \right).$$

The adjoint of the projection map $(x, y, z) \mapsto (x, y)$ is given by the inclusion $(x, y) \mapsto (x, y, 0)$. Thus, the adjoint of the map $\pi : A \rightarrow \mathbb{R}^{2 \times N}$, which is given by a projection on each component,

is obtained by including each of the components of $\mathbb{R}^{2 \times N}$ into \mathbb{R}^3 . The adjoint of the projection map $(x, y, z) \mapsto (x, y)$ is given by the matrix-vector product

$$\Lambda \begin{pmatrix} x \\ y \\ 0 \end{pmatrix} = \begin{pmatrix} x \\ y \\ 0 \end{pmatrix} \quad \text{where} \quad \Lambda = \begin{pmatrix} 1 & 0 \\ 0 & 1 \\ 0 & 0 \end{pmatrix}.$$

The extension to $\mathbb{R}^{2 \times N}$ is the linear map $\Lambda \oplus \dots \oplus \Lambda: \mathbb{R}^{2 \times N} \rightarrow A$ obtained by applying Λ to each component.

Finally, we calculate the adjoint of $d(\mathcal{B}_{2D})_q: \mathbb{R}^{2 \times N} \rightarrow Y$. Differentiating \mathcal{B}_{2D} at an arbitrary point $q \in \mathbb{R}^{2 \times N}$ gives

$$d(\mathcal{B}_{2D})_q(q') = \sum_{i=1}^N \langle -q'_i, s_i \tau_{q_i} \nabla \varphi_{\sigma_i} \rangle = \sum_{i=1}^N \langle q'_i, -s_i \tau_{q_i} \nabla \varphi_{\sigma_i} \rangle \quad \text{for } q' \in \mathbb{R}^{2 \times N}.$$

Thus, if $y \in Y$, we have

$$\langle d(\mathcal{B}_{2D})_q(q'), y \rangle_Y = \sum_{i=1}^N \left\langle q'_i, -s_i \int_{\mathbb{R}^2} y \tau_{q_i} \nabla \varphi_{\sigma_i} \right\rangle = \sum_{i=1}^N \langle q'_i, s_i (y * \nabla \varphi_{\sigma_i})(q_i) \rangle.$$

The second equality above follows from the following identity;

$$- \int_{\mathbb{R}^2} y \tau_{q_i} \nabla \varphi_{\sigma_i} = (y * \nabla \varphi_{\sigma_i})(q_i)$$

which holds since the gradient of an even function (in our case: the Gaussian probability density function) is odd. Furthermore, the integral above acts component wise on the integrand, and $(y * \nabla \varphi_{\sigma_i})(q_i)$ is the convolution of y with $\nabla \varphi_{\sigma_i}$ evaluated at the point q_i . \blacksquare

Appendix C. An existence result. This section formulates the minimization of (2.4) over \mathcal{L}^2 curves in the Lie algebra \mathfrak{g} following [94]. The existence of a minimizer can be proven in the same way as in the proof of [22, Theorem 7.4]. Most of the results stated here are special cases of more general results found in [94], but the proofs in our specific setting are simpler.

Let \mathbb{M} be the space of complex $n \times n$ -matrices equipped with the operator norm $\|\cdot\|$. Note that \mathbb{M} is finite dimensional, so the operator norm topology is the same as the one induced by an inner product, for example. The operator norm makes the proofs in this appendix easier, which is why we have chosen this norm. The Banach space $\mathcal{L}^2([0, 1], \mathbb{M})$ is defined as the space of all measurable curves $\nu: [0, 1] \rightarrow \mathbb{M}$ such that

$$\int_0^1 \|\nu(s)\|_{\mathbb{M}}^2 ds < \infty.$$

Given a curve $\nu \in \mathcal{L}^2([0, 1], \mathbb{M})$, we say that a continuous curve $\gamma: [0, 1] \rightarrow \mathbb{M}$ is a solution to the differential equation $\dot{\gamma} = \nu \gamma$ with initial condition $\gamma(0) = e$ (special case of (2.3) when $G \subset \mathbb{M}$), in which e is the identity matrix, if

$$\gamma(t) = e + \int_0^t \nu(s) \gamma(s) ds.$$

The existence and uniqueness of solutions to the differential equation is guaranteed by [94, Corollary C.7]. We shall often write γ^ν for this unique solution to emphasize the dependence on ν .

We now show that the map $\nu \mapsto \gamma^\nu(t)$ is weakly continuous for any $t \in [0, 1]$, which in principle follows from [94, Section 7.2.4].

Proposition C.1. *Let \mathbb{M} be the space of complex $n \times n$ -matrices. For any fixed $t \in [0, 1]$, the map $\mathcal{L}^2([0, 1], \mathbb{M}) \ni \nu \mapsto \gamma^\nu(t) \in \mathbb{M}$, is weakly continuous on the closed unit ball of $\mathcal{L}^2([0, 1], \mathbb{M})$.*

Proof. Take $\nu_1, \nu_2 \in \mathcal{L}^2([0, 1], \mathbb{M})$ with $\|\nu_2\| \leq 1$. Write $\gamma_i = \gamma^{\nu_i}$ for ease of notation. By definition, it holds that

$$\gamma_i(t) = e + \int_0^t \nu_i(s) \gamma_i(s) ds.$$

Then

$$\begin{aligned} \|\gamma_2(t) - \gamma_1(t)\| &\leq \left\| \int_0^t (\nu_1(s) - \nu_2(s)) \gamma_1(s) ds \right\| + \int_0^t \|\nu_2(s) (\gamma_1(s) - \gamma_2(s))\| ds \\ &= \|\Lambda_t(\nu_1 - \nu_2)\| + \int_0^t \|\nu_2(s) (\gamma_1(s) - \gamma_2(s))\| ds. \end{aligned}$$

where $\Lambda_t(\nu) = \int_0^t \nu(s) \gamma_1(s) ds$ defines a bounded linear map $\Lambda_t : \mathcal{L}^2([0, 1], \mathbb{M}) \rightarrow \mathbb{M}$. From Grönwall's lemma and the assumption $\|\nu_2\| \leq 1$, it follows that

$$\|\gamma_2(t) - \gamma_1(t)\| \leq \|\Lambda_t(\nu_1 - \nu_2)\| e^{\int_0^t \|\nu_2(s)\| ds} \leq \|\Lambda_t(\nu_1 - \nu_2)\| e^{\sqrt{t}}.$$

Since the map Λ_t is bounded and has finite dimensional codomain, it is weakly continuous (note that boundedness implies continuity with respect to the weak topology on both domain and codomain, and since the codomain is finite dimensional the map is also continuous with respect to the weak topology on the domain and the norm topology on the codomain). Thus, for any $\varepsilon > 0$ there is a weakly open neighborhood U of ν_1 such that $\|\gamma_1(t) - \gamma_2(t)\| < \varepsilon$ if $\nu_2 \in U$. It follows that the restriction of $\nu \mapsto \gamma^\nu(t)$ to the closed unit ball is weakly continuous. \blacksquare

Our next results show that if ν lies in a Lie algebra of a matrix Lie group that is closed in \mathbb{M} (such as $\text{SO}(3)$), then the corresponding solution γ^ν lies in the group.

Proposition C.2. *Suppose $G \subset \mathbb{M}$ is a closed matrix Lie group. If $\nu \in \mathcal{L}^2([0, 1], \mathfrak{g})$, then the unique continuous solution $\gamma^\nu : [0, 1] \rightarrow \mathbb{M}$ to $\dot{\gamma} = \nu\gamma$ with initial condition $\gamma(0) = e$ is a curve in G .*

Proof. In the case that ν is smooth, we have that there exists for each $p \in G$ a unique integral curve $\gamma : J \rightarrow G$ for some open interval J containing 0, of the smooth time-dependent vector field $W(t, g) = \nu(t)g$ on G starting at p . Note that W extends to a smooth vector field on \mathbb{M} , so any integral curve of W in \mathbb{M} that starts at a point of G stays in G , at least for small enough times, by uniqueness of integral curves.

By the definition of γ^ν and an induction argument, γ^ν is smooth and thus is a smooth integral curve of W .

By the above, the set A of points in $[0, 1]$ that γ^ν maps into G is open. Since $A = (\gamma^\nu)^{-1}(G)$ the set is closed by continuity. Since $0 \in A$, we conclude that $A = [0, 1]$.

In general, if $\nu \in \mathcal{L}^2([0, 1], \mathfrak{g})$, there exists a sequence of smooth curves (ν_k) that converges to ν in $\mathcal{L}^2([0, 1], \mathfrak{g})$. Since the map $\nu \mapsto \gamma^\nu(t)$ for any fixed $t \in [0, 1]$ is weakly continuous, as we saw in the previous proposition, it follows that every point $\gamma^\nu(t)$ lies arbitrarily close to G . As G is closed, we must have $\gamma^\nu(t) \in G$. ■

The above proposition shows that $\nu \mapsto \gamma^\nu(1)$ maps $\mathcal{L}^2([0, 1], \mathfrak{g})$ into G . This result will be used implicitly in what follows.

Let V and Y be topological spaces, and assume that the group G acts continuously on V via $\Phi: G \times V \rightarrow V$. For a map $\mathcal{D}: V \times Y \rightarrow [0, \infty)$, a constant $\lambda > 0$, and fixed elements $w \in V$ and $y \in Y$ we shall consider the functional

$$\mathcal{E}(\nu) = \mathcal{D}(\Phi(\gamma^\nu(1), w), y) + \lambda \|\nu\|_2^2,$$

which maps $\mathcal{L}^2([0, 1], \mathfrak{g})$ into $[0, \infty)$. We can now prove the existence of a minimizer of (2.8), using the same method as in the proof of Theorem 7.4 in [22]. Note that we do this under slightly weaker conditions on \mathcal{D} than we actually have in (2.8).

Theorem C.3. *If $\mathcal{D}(\cdot, y)$ is lower semi-continuous on V , then there exists an element $\tilde{\nu} \in \mathcal{L}^2([0, 1], \mathfrak{g})$ such that*

$$\mathcal{E}(\tilde{\nu}) = \inf_{\nu \in \mathcal{L}^2([0, 1], \mathfrak{g})} \mathcal{E}(\nu).$$

Proof. Let $\alpha = \inf_{\nu \in \mathcal{L}^2([0, 1], \mathfrak{g})} \mathcal{E}(\nu)$ and let (ν_k) be a sequence such that $\mathcal{E}(\nu_k) \rightarrow \alpha$. Since $\lambda > 0$, the sequence (ν_k) is bounded. Furthermore, since \mathfrak{g} is finite dimensional, $\mathcal{L}^2([0, 1], \mathfrak{g})$ is separable, and it follows from the Banach–Alaoglu theorem that there is a subsequence such that (ν_k) converges weakly to some $\tilde{\nu} \in \mathcal{L}^2([0, 1], \mathfrak{g})$. By C.1, we have that $\gamma^{\nu_k}(1) \rightarrow \gamma^{\tilde{\nu}}(1)$. Now, the identity $\mathcal{E}(\tilde{\nu}) = \alpha$ follows directly from the following calculation:

$$\begin{aligned} \alpha &= \lim_{k \rightarrow \infty} \mathcal{E}(\nu_k) \geq \liminf_{k \rightarrow \infty} \mathcal{D}(\Phi(\gamma^{\nu_k}(1), w), y) + \lambda \liminf_{k \rightarrow \infty} \|\nu_k\|_2^2 \\ &\geq \mathcal{D}(\Phi(\gamma^{\tilde{\nu}}(1), w), y) + \lambda \liminf_{k \rightarrow \infty} \|\nu_k\|_2^2 \geq \mathcal{D}(\Phi(\gamma^{\tilde{\nu}}(1), w), y) + \lambda \|\tilde{\nu}\|_2^2 = \mathcal{E}(\tilde{\nu}) \geq \alpha. \quad \blacksquare \end{aligned}$$

REFERENCES

- [1] J. ABRAMSON, J. ADLER, J. DUNGER, R. EVANS, T. GREEN, A. PRITZEL, O. RONNEBERGER, L. WILLMORE, A. J. BALLARD, J. BAMBRICK, S. W. BODENSTEIN, D. A. EVANS, C.-C. HUNG, M. O’NEILL, D. REIMAN, K. TUNYASUVUNAKOOL, Z. WU, A. ŽEMGULYTĖ, E. ARVANITI, C. BEATTIE, O. BERTOLLI, A. BRIDGLAND, A. CHEREPANOV, M. CONGREVE, A. I. COWEN-RIVERS, A. COWIE, M. FIGURNOV, F. B. FUCHS, H. GLADMAN, R. JAIN, Y. A. KHAN, C. M. R. LOW, K. PERLIN, A. POTAPENKO, P. SAVY, S. SINGH, A. STECULA, A. THILLAISUNDARAM, C. TONG, S. YAKNEEN, E. D. ZHONG, M. ZIELINSKI, A. ŽÍDEK, V. BAPST, P. KOHLI, M. JADERBERG, D. HASSABIS, AND J. M. JUMPER, *Accurate structure prediction of biomolecular interactions with AlphaFold 3*, Nature, 630 (2024), pp. 493–500, <https://doi.org/10.1038/s41586-024-07487-w>.

- [2] M. ADRIAN, J. DUBOCHET, J. LEPAULT, AND A. W. MCDOWALL, *Cryo-electron microscopy of viruses*, Nature, 308 (1984), pp. 32–36, <https://doi.org/10.1038/308032a0>.
- [3] B. ALBERTS, A. JOHNSON, J. LEWIS, M. RAFF, K. ROBERTS, AND P. WALTER, *Molecular Biology of the Cell*, Garland Publishing, New York, 6 ed., November 2014, <https://doi.org/10.3390/ijms161226074>.
- [4] X.-C. BAI, G. MCMULLAN, AND S. H. W. SCHERES, *How cryo-EM is revolutionizing structural biology*, Trends in biochemical sciences, 40 (2015), pp. 49–57, <https://doi.org/10.1016/j.tibs.2014.10.005>.
- [5] T. S. BAKER AND H. R. CHENG, *A model-based approach for determining orientations of biological macromolecules imaged by cryoelectron microscopy*, Journal of Structural Biology, 116 (1996), pp. 120–130, <https://doi.org/10.1006/jsbi.1996.0020>.
- [6] T. BALEHOWSKY, C.-J. KARLSSON, AND K. MODIN, *Shape analysis via gradient flows on diffeomorphism groups*, Nonlinearity, 36 (2022), p. 862, <https://doi.org/10.1088/1361-6544/aca73c>.
- [7] O. BECKSTEIN, S. L. SEYLER, AND A. KUMAR, *Simulated trajectory ensembles for the closed-to-open transition of adenylate kinase from DIMS MD and FRODA*, 2018.
- [8] F. BEG, M. MILLER, A. TROUVÉ, AND L. YOUNES, *Computing large deformation metric mappings via geodesic flows of diffeomorphisms*, International Journal of Computer Vision, 61 (2005), pp. 139–157, <https://doi.org/10.1023/b:visi.0000043755.93987.aa>, <http://dx.doi.org/10.1023/b:visi.0000043755.93987.aa>.
- [9] T. BENDORY, A. BARTESAGHI, AND A. SINGER, *Single-particle cryo-electron microscopy: Mathematical theory, computational challenges, and opportunities*, IEEE signal processing magazine, 37 (2020), pp. 58–76, <https://doi.org/10.1109/MSP.2019.2957822>.
- [10] X. BENJI AND L. LING, *Developments, applications, and prospects of cryo-electron microscopy*, Protein Science, 29 (2020), pp. 872–882, <https://doi.org/10.1002/pro.3805>.
- [11] S. I. BHUYAN AND X. GAO, *A protein-dependent side-chain rotamer library*, BMC Bioinformatics, 12 (2011), p. S10, <https://doi.org/10.1186/1471-2105-12-S14-S10>.
- [12] N. BOUMAL, *An introduction to optimization on smooth manifolds*, Cambridge University Press, 2023, <https://doi.org/10.1017/9781009166164>.
- [13] G. BOUVIER, B. BARDIAUX, R. PELLARIN, C. RAPISARDA, AND M. NILGES, *Building protein atomic models from cryo-EM density maps and residue co-evolution*, Biomolecules, 12 (2022), p. 1290, <https://doi.org/10.3390/biom12091290>, <http://dx.doi.org/10.3390/biom12091290>.
- [14] A. BROWAND, F. LONG, R. A. NICHOLLS, J. TOOTS, P. EMSLEY, AND G. MURSHUDOV, *Tools for macromolecular model building and refinement into electron cryo-microscopy reconstructions*, Acta Crystallographica Section D: Structural Biology, 71 (2015), pp. 136–153, <https://doi.org/10.1107/S1399004714021683>.
- [15] M. BRUVERIS AND D. D. HOLM, *Geometry of Image Registration: The Diffeomorphism Group and Momentum Maps*, Springer, 2015, pp. 19–56, https://doi.org/10.1007/978-1-4939-2441-7_2, http://dx.doi.org/10.1007/978-1-4939-2441-7_2.
- [16] R. H. BYRD, P. LU, J. NOCEDAL, AND C. ZHU, *A limited memory algorithm for bound constrained optimization*, SIAM Journal of Scientific Computing, 16 (1995), pp. 1190–1208, <https://doi.org/10.1137/0916069>, <http://dx.doi.org/10.1137/0916069>.
- [17] J. M. CARAZO, C. O. S. SORZANO, J. OTÓN, R. MARABINI, AND J. VARGAS, *Three-dimensional reconstruction methods in single particle analysis from transmission electron microscopy data*, Archives of Biochemistry and Biophysics, 581 (2015), pp. 39–48, <https://doi.org/10.1016/j.abb.2015.05.003>.
- [18] A. CASAÑAL, B. LOHKAMP, AND P. EMSLEY, *Current developments in coot for macromolecular model building of electron cryo-microscopy and crystallographic data*, Protein Science, 29 (2020), pp. 1069–1078, <https://doi.org/10.1002/pro.3791>.
- [19] C. CERITOGU, X. TANG, M. CHOW, D. HADJIABADI, D. SHAH, T. BROWN, M. BURHANULLAH, H. TRINH, J. HSU, K. AMENT, D. CROCETTI, S. MORI, S. MOSTOFKY, S. YANTIS, M. MILLER, AND T. RATNANATHER, *Computational analysis of LDDMM for brain mapping*, Frontiers in Neuroscience, 7 (2013), p. 151, <https://doi.org/10.3389/fnins.2013.00151>, <https://www.frontiersin.org/article/10.3389/fnins.2013.00151>.
- [20] C. CHEN, B. GRIS, AND O. ÖKTEM, *A new variational model for joint image reconstruction and motion estimation in spatiotemporal imaging*, SIAM Journal on Imaging Sciences, 12 (2019), pp. 1686–1719, <https://doi.org/10.1137/18M1234047>.
- [21] C. CHEN AND O. ÖKTEM, *Indirect image registration with large diffeomorphic deformations*, SIAM Jour-

- nal on Imaging Sciences, 11 (2018), pp. 575–617, <https://doi.org/10.1137/17M113462>.
- [22] C. CHEN AND O. ÖKTEM, *Indirect image registration with large diffeomorphic deformations*, SIAM Journal of Imaging Science, 11 (2018), pp. 575–617, <https://doi.org/10.1137/17m1134627>, <http://dx.doi.org/10.1137/17M1134627>.
- [23] A. CHENG AND Y. YU, *Recent advances in data collection for Cryo-EM methods*, Current Opinion in Structural Biology, 86 (2024), p. 102795, <https://doi.org/10.1016/j.sbi.2024.102795>.
- [24] Y. CHENG, *Single-particle Cryo-EM at crystallographic resolution*, Cell, 163 (2015), pp. 450–457, <https://doi.org/10.1016/j.cell.2015.03.049>.
- [25] Y. CHENG, *Single-particle cryo-em—how did it get here and where will it go*, Science, 361 (2018), pp. 876–880, <https://doi.org/10.1126/science.aat43>, <https://doi.org/10.1126/science.aat43>. Special issue: Technologies Transforming Biology.
- [26] Y. CHENG, N. GRIGORIEFF, P. A. PENCZEK, AND T. WALZ, *A primer to single-particle cryo-electron microscopy.*, Cell, 161 (2015), pp. 438–449., <https://doi.org/10.1016/j.cell.2015.03.050>.
- [27] G. CHOJNOWSKI, E. SOBOLEV, P. HEUSER, AND V. S. LAMZIN, *The accuracy of protein models automatically built into cryo-EM maps with ARP/wARP*, Acta Crystallographica Section D: Structural Biology, 77 (2021), pp. 142–150, <https://doi.org/10.1107/S2059798320016332>.
- [28] M. R. CORUM, H. VENKANNAGARI, C. F. HRYC, AND M. L. BAKER, *Predictive modeling and cryo-EM: A synergistic approach to modeling macromolecular structure*, Biophysical Journal, 123 (2024), pp. 435–450, <https://doi.org/10.1016/j.bpj.2024.01.021>.
- [29] W. DIEPEVEEN, C. ESTEVE-YAGÜE, J. LELLMANN, O. ÖKTEM, AND C.-B. SCHÖNLIEB, *Riemannian geometry for efficient analysis of protein dynamics data*, Proceedings of the National Academy of Sciences of the United States of America (PNAS), 121 (2024), p. e2318951121, <https://doi.org/10.1073/pnas.2318951121>.
- [30] W. DIEPEVEEN, J. LELLMANN, O. ÖKTEM, AND C.-B. SCHÖNLIEB, *Regularizing orientation estimation in cryogenic electron microscopy three-dimensional map refinement through measure-based lifting over Riemannian manifolds*, SIAM Journal of Imaging Science, 16 (2023), pp. 1440–1490, <https://doi.org/10.1137/22m1520773>, <http://dx.doi.org/10.1137/22M1520773>.
- [31] W. DIEPEVEEN, J. LELLMANN, O. ÖKTEM, AND C.-B. SCHÖNLIEB, *Regularizing orientation estimation in cryogenic electron microscopy three-dimensional map refinement through measure-based lifting over riemannian manifolds*, SIAM Journal on Imaging Sciences, 16 (2023), pp. 1440–1490, <https://doi.org/10.1137/22M1520773>.
- [32] J. DUBOCHET, J. LEPAULT, R. FREEMAN, J. A. BERRIMAN, AND J.-C. HOMO, *Electron microscopy of frozen water and aqueous solutions*, Journal of Microscopy, 128 (1982), pp. 219–237, <https://doi.org/10.1111/j.1365-2818.1982.tb04625.x>.
- [33] R. L. DUNBRACK AND M. KARPLUS, *Backbone-dependent rotamer library for proteins. application to side-chain prediction*, Journal of Molecular Biology, 230 (1993), pp. 543–574, <https://doi.org/10.1006/jmbi.1993.1170>.
- [34] C. ESTEVE-YAGÜE, W. DIEPEVEEN, O. ÖKTEM, AND C.-B. SCHÖNLIEB, *Spectral decomposition of atomic structures in heterogeneous cryo-EM*, Inverse Problems, 39 (2023), p. 034003, <https://doi.org/10.1088/1361-6420/acb2ba>, <http://dx.doi.org/10.1088/1361-6420/acb2ba>.
- [35] R. EVANS, M. O’NEILL, N. A. ALEXANDER PRITZEL, A. SENIOR, A. Ž. TIM GREEN, R. BATES, S. BLACKWELL, J. YIM, O. RONNEBERGER, A. B. SEBASTIAN BODENSTEIN, MICHAL ZIELINSKI, A. POTAPENKO, A. COWIE, K. TUNYASUVUNAKOOL, R. JAIN, E. CLANCY, P. KOHLI, J. JUMPER, AND D. HASSABIS, *Protein complex prediction with AlphaFold-Multimer*, bioRxiv, (2022), <https://doi.org/10.1101/2021.10.04.463034>.
- [36] D. FANELLI AND O. ÖKTEM, *Electron tomography: a short overview with an emphasis on the absorption potential model for the forward problem*, Inverse Problems, 24 (2008), p. 013001, <https://doi.org/10.1088/0266-5611/24/1/013001>, <http://dx.doi.org/10.1088/0266-5611/24/1/013001>.
- [37] A. R. FARUQI, R. HENDERSON, AND G. MCMULL, *Progress and development of direct detectors for electron cryomicroscopy*, Advances in Imaging and Electron Physics, 190 (2015), pp. 103–141, <https://doi.org/10.1016/bs.aiep.2015.03.002>.
- [38] J. FRANK, *Averaging of low exposure electron micrographs of non-periodic objects*, Ultramicroscopy, 1 (1975), pp. 159–162, [https://doi.org/10.1016/S0304-3991\(75\)80020-9](https://doi.org/10.1016/S0304-3991(75)80020-9), [https://doi.org/10.1016/S0304-3991\(75\)80020-9](https://doi.org/10.1016/S0304-3991(75)80020-9).

- [39] J. FRANK, *Three-Dimensional Electron Microscopy of Macromolecular Assemblies: Visualization of Biological Molecules in Their Native State*, Oxford University Press, 2006, <https://doi.org/10.1093/acprof:oso/9780195182187.001.0001>.
- [40] N. GIRI AND J. CHENG, *De novo atomic protein structure modeling for cryoEM density maps using 3D transformer and HMM*, Nature Communications, 15 (2024), p. 5511, <https://doi.org/10.1038/s41467-024-49647-6>.
- [41] N. GIRI, R. S. ROY, AND J. CHENG, *Deep learning for reconstructing protein structures from cryo-EM density maps: Recent advances and future directions*, Current Opinion in Structural Biology, 79 (2023), p. 102536, <https://doi.org/10.1016/j.sbi.2023.102536>.
- [42] N. GIRI, L. WANG, AND J. CHENG, *Cryo2StructData: A large labeled Cryo-EM density map dataset for ai-based modeling of protein structures*, Scientific Data, 11 (2024), p. 458, <https://doi.org/10.1038/s41597-024-03299-9>.
- [43] J. C. GOWER, *Generalized Procrustes analysis*, Psychometrika, 40 (1975), pp. 33–51, <https://doi.org/10.1007/bf02291478>, <http://dx.doi.org/10.1007/BF02291478>.
- [44] U. GRENANDER, *General Pattern Theory*, Clarendon Press, Oxford, 1993, <https://doi.org/10.1093/oso/9780198536710.001.0001>.
- [45] U. GRENANDER AND M. MILLER, *Pattern theory: from representation to inference*, Oxford University Press, Oxford, 2007, <https://doi.org/10.1093/oso/9780198505709.001.0001>.
- [46] B. GRIS, C. CHEN, AND O. ÖKTEM, *Image reconstruction through metamorphosis*, Inverse Problems, 36 (2020), p. 025001, <https://doi.org/10.1088/1361-6420/ab5832>.
- [47] M. GROMOV, *Crystals, proteins, stability and isoperimetry*, Bulletin of the American Mathematical Society, 48 (2011), pp. 229–257, <https://doi.org/10.1090/S0273-0979-2010-01319-7>.
- [48] A. HAUPTMANN, O. ÖKTEM, AND C.-B. SCHÖNLIEB, *Image reconstruction in dynamic inverse problems with temporal models*, in Handbook of Mathematical Models and Algorithms in Computer Vision and Imaging: Mathematical Imaging and Vision, K. Chen, C.-B. Schönlieb, X.-C. Tai, and L. Younes, eds., Springer Verlag, 2023, pp. 1707–1737, https://doi.org/10.1007/978-3-030-98661-2_83.
- [49] J. HE, T. LI, AND S.-Y. HUANG, *Improvement of cryo-EM maps by simultaneous local and non-local deep learning*, Nature Communications, 14 (2023), p. 3217, <https://doi.org/10.1038/s41467-023-39031-1>.
- [50] J. HE, P. LIN, J. CHEN, H. CAO, AND S.-Y. HUANG, *Model building of protein complexes from intermediate-resolution cryo-EM maps with deep learning-guided automatic assembly*, Nature Communications, 13 (2022), p. 4066, <https://doi.org/10.1038/s41467-022-31748-9>.
- [51] M. V. HEEL, *Angular reconstitution: A posteriori assignment of projection directions for 3D reconstruction*, Ultramicroscopy, 21 (1987), pp. 111–123, [https://doi.org/10.1016/0304-3991\(87\)90078-7](https://doi.org/10.1016/0304-3991(87)90078-7).
- [52] M. V. HEEL AND J. FRANK, *Use of multivariate statistics in analysing the images of biological macromolecules*, Ultramicroscopy, 6 (1981), pp. 187–194, [https://doi.org/10.1016/S0304-3991\(81\)80197-0](https://doi.org/10.1016/S0304-3991(81)80197-0).
- [53] M. A. HERZIK, *Cryo-electron microscopy reaches atomic resolution*, Nature, 587 (2020), pp. 39–40, <https://doi.org/10.1038/d41586-020-02924-y>.
- [54] A. ISERLES, H. Z. MUNTHE-KAAS, S. P. NØRSETT, AND A. ZANNA, *Lie-group methods*, Acta Numerica, 9 (2000), pp. 215–365, <https://doi.org/10.1017/S0962492900002154>.
- [55] K. JAMALI, L. KÄLL, R. ZHANG, A. BROWN, D. KIMANIUS, AND S. H. W. SCHERES, *Automated model building and protein identification in cryo-EM maps*, Nature, 628 (2024), pp. 450–457, <https://doi.org/10.1038/s41586-024-07215-4>.
- [56] J. JUMPER, R. EVANS, A. PRITZEL, T. GREEN, M. FIGURNOV, O. RONNEBERGER, K. TUNYASUVUNAKOOL, R. BATES, A. ŽÍDEK, A. POTAPENKO, A. BRIDGLAND, C. MEYER, S. A. A. KOHL, A. J. BALLARD, A. COWIE, B. ROMERA-PAREDES, S. NIKOLOV, R. JAIN, J. ADLER, T. BACK, S. PETERSEN, D. REIMAN, E. CLANCY, M. ZIELINSKI, M. STEINEGGER, M. PACHOLSKA, T. BERGHAMMER, S. BODENSTEIN, D. SILVER, O. VINYALS, A. W. SENIOR, K. KAVUKCUOGLU, P. KOHLI, AND D. HASSABIS, *Highly accurate protein structure prediction with AlphaFold*, Nature, 596 (2021), pp. 583–589, <https://doi.org/10.1038/s41586-021-03819-2>, <http://dx.doi.org/10.1038/s41586-021-03819-2>.
- [57] D. G. KENDALL, *A survey of the statistical theory of shape*, Statistical Science, 4 (1989), <https://doi.org/10.1214/ss/1177012582>, <http://dx.doi.org/10.1214/ss/1177012582>.
- [58] N. LIU AND H.-W. WANG, *Better Cryo-EM specimen preparation: How to deal with the air-water interface?*, Journal of Molecular Biology, 435 (2023), p. 167926, <https://doi.org/10.1016/j.jmb.2022>.

- 167926.
- [59] S. MALHOTRA, S. TRÄGER, M. D. PERARO, AND M. TOPF, *Modelling structures in cryo-EM maps*, *Current Opinion in Structural Biology*, 58 (2019), pp. 105–114, <https://doi.org/10.1016/j.sbi.2019.05.024>.
- [60] J. E. MARSDEN AND T. RATIU, *Introduction to Mechanics and Symmetry*, Springer, 1999, <https://doi.org/10.1007/978-0-387-21792-5>.
- [61] E. C. MENG, T. D. GODDARD, E. F. PETERSEN, G. S. COUCH, Z. J. PEARSON, J. H. MORRIS, AND T. E. FERRIN, *UCSF ChimeraX: Tools for structure building and analysis*, *Protein Science*, 32 (2023), p. e4792, <https://doi.org/10.1002/pro.4792>.
- [62] G. N. MURSHUDOV, *Refinement of atomic structures against cryo-EM maps*, *Methods in Enzymology*, 579 (2016), pp. 277–305, <https://doi.org/10.1016/bs.mie.2016.05.033>.
- [63] T. NAKANE, A. KOTECHEA, A. SENTÉ, G. McMULLAN, S. MASIULIS, P. M. G. E. BROWN, I. T. GRIGORAS, L. MALINAUSKAITE, T. MALINAUSKAS, J. MIEHLING, T. UCHAŃSKI, L. YU, D. KARIA, E. V. PECHNIKOVA, E. DE JONG, J. KEIZER, M. BISCHOFF, J. McCORMACK, P. TIEMEIJER, S. W. HARDWICK, D. Y. CHIRGADZE, G. MURSHUDOV, A. R. ARICESCU, AND S. H. W. SCHERES, *Single-particle cryo-EM at atomic resolution*, *Nature*, 587 (2020), pp. 152–156, <https://doi.org/10.1038/s41586-020-2829-0>, <http://dx.doi.org/10.1038/s41586-020-2829-0>.
- [64] E. NOGALES, *The development of cryo-EM into a mainstream structural biology technique*, *Nature Methods*, 13 (2016), pp. 24–27, <https://doi.org/10.1038/nmeth.3694>.
- [65] E. NOGALES AND S. H. W. SCHERES, *Cryo-EM: A unique tool for the visualization of macromolecular complexity*, *Molecular Cell*, 58 (2015), pp. 677–689, <https://doi.org/10.1016/j.molcel.2015.02.019>.
- [66] O. ÖKTEM, *Mathematics of Electron Tomography*, Springer, 2015, pp. 937–1031, https://doi.org/10.1007/978-1-4939-0790-8_43, http://dx.doi.org/10.1007/978-1-4939-0790-8_43.
- [67] O. ÖKTEM, C. CHEN, N. O. DOMANIC, P. RAVIKUMAR, AND C. BAJAJ, *Shape-based image reconstruction using linearized deformations*, *Inverse Problems*, 33 (2017), p. 035004, <https://doi.org/10.1088/1361-6420/aa55af>.
- [68] P. A. PENCZEK, G. R. A. AND J. FRANK, *The Ribosome at improved resolution: new techniques for merging and orientation refinement in 3D cryo-electron microscopy of biological particles*, *Ultramicroscopy*, 53 (1994), pp. 251–270., [https://doi.org/10.1016/0304-3991\(94\)90038-8](https://doi.org/10.1016/0304-3991(94)90038-8).
- [69] J.-P. RENAUD, A. CHARI, C. CIFERRI, W. TI LIU, H.-W. RÉMIGY, H. STARK, AND C. WIESMANN, *Cryo-EM in drug discovery: achievements and limitations and prospects*, *Nature Reviews Drug Discovery*, 17 (2018), pp. 471–492, <https://doi.org/10.1038/nrd.2018.77>.
- [70] L. RISSER, F. VIALARD, H. Y. BALUWALA, AND J. SCHNABEL, *Piecewise-diffeomorphic image registration: Application to the motion estimation between 3D CT lung images with sliding conditions*, *Medical Image Analysis*, 17 (2013), pp. 182–193, <https://doi.org/10.1016/j.media.2012.10.001>, <https://doi.org/10.1016/j.media.2012.10.001>.
- [71] M. J. ROBERTSON, J. G. MEYEROWITZ, AND G. SKINIOTIS, *Drug discovery in the era of cryo-electron microscopy*, *Trends in Biochemical Sciences*, 47 (2022), pp. 124–135, <https://doi.org/10.1016/j.tibs.2021.06.008>.
- [72] D. ROSENBAUM, M. GARNELO, M. ZIELINSKI, C. BEATTIE, E. CLANCY, A. HUBER, P. KOHLI, A. W. SENIOR, J. JUMPER, C. DOERSCH, S. M. A. ESLAMI, O. RONNEBERGER, AND J. ADLER, *Inferring a continuous distribution of atom coordinates from Cryo-EM images using VAEs*, 2021, <https://arxiv.org/abs/2106.14108>.
- [73] D. J. D. ROSIER AND A. KLUG, *Reconstruction of three dimensional structures from electron micrographs*, *Nature*, 217 (1968), pp. 130–134, <https://doi.org/10.1038/217130a0>.
- [74] H. RULLGÅRD, L.-G. ÖFVERSTEDT, S. MASICH, B. DANEHOLT, AND O. ÖKTEM, *Simulation of transmission electron microscope images of biological specimens*, *Inverse Problems*, 243 (2011), pp. 234–256, <https://doi.org/10.1111/j.1365-2818.2011.03497.x>, <https://doi.org/10.1111/j.1365-2818.2011.03497.x>.
- [75] S. H. W. SCHERES, *A Bayesian view on cryo-EM structure determination*, *Journal of Molecular Biology*, 415 (2012), pp. 406–418, <https://doi.org/10.1016/j.jmb.2011.11.010>.
- [76] S. H. W. SCHERES, *RELION: implementation of a Bayesian approach to cryo-EM structure determination*, *Journal of Structural Biology*, 180 (2012), pp. 519–530, <https://doi.org/10.1016/j.jsb.2012.09.006>.

- [77] S. L. SEYLER, A. KUMAR, M. F. THORPE, AND O. BECKSTEIN, *Path similarity analysis: A method for quantifying macromolecular pathways*, PLOS Computational Biology, 11 (2015), p. e1004568, <https://doi.org/10.1371/journal.pcbi.1004568>, <http://dx.doi.org/10.1371/journal.pcbi.1004568>.
- [78] D. SI, S. A. MORITZ, J. PFAB, J. HOU, R. CAO, L. WANG, T. WU, AND J. CHENG, *Deep learning to predict protein backbone structure from high-resolution Cryo-EM density maps*, Scientific Reports, 10 (2020), p. 4282, <https://doi.org/10.1038/s41598-020-60598-y>.
- [79] F. J. SIGWORTH, *A maximum-likelihood approach to single-particle image refinement*, Journal of Structural Biology, 122 (1998), pp. 328–339, <https://doi.org/10.1006/jsbi.1998.4014>.
- [80] F. J. SIGWORTH, *Principles of cryo-EM single-particle image processing*, Microscopy, 65 (2016), pp. 57–67, <https://doi.org/10.1093/jmicro/dfv370>.
- [81] F. J. SIGWORTH, P. C. DOERSCHUK, J.-M. CARAZO, AND S. H. W. SCHERES, *An introduction to maximum-likelihood methods in Cryo-EM*, Methods in Enzymology, 482 (2010), pp. 263–294, [https://doi.org/10.1016/S0076-6879\(10\)82011-7](https://doi.org/10.1016/S0076-6879(10)82011-7).
- [82] A. SINGER, *Mathematics for cryo-electron microscopy*, in Proceedings of the International Congress of Mathematicians 2018, vol. 4, 2018, pp. 4013–4032, https://doi.org/10.1142/9789813272880_0209.
- [83] A. SINGER AND F. J. SIGWORTH, *Computational methods for single-particle electron cryomicroscopy*, Annual Review of Biomedical Data Science, 3 (2020), pp. 163–190, <https://doi.org/10.1146/annurev-biodatasci-021020-093826>.
- [84] C. O. S. SORZANO, J. VARGAS, J. OTÓN, J. M. DE LA ROSA-TREVÍN, J. L. VILAS, M. KAZEMI, R. MELERO, L. D. CAÑO, J. CUENCA, P. CONESA, J. GÓMEZ-BLANCO, R. MARABINI, AND J. M. CARAZO, *A survey of the use of iterative reconstruction algorithms in electron microscopy*, BioMed Research International, (2017), <https://doi.org/10.1155/2017/6482567>.
- [85] C. TAYLOR AND D. KRIEGMAN, *Minimization on the lie group SO(3) and related manifolds*, tech. report, Yale University, 1994. Tech. Rep. 9405.
- [86] W. R. TAYLOR, A. C. W. MAY, N. P. BROWN, AND A. ASZÓDI, *Protein structure: geometry, topology and classification*, Reports on Progress in Physics, 64 (2001), pp. 517–590, <https://doi.org/10.1088/0034-4885/64/4/203>, <http://dx.doi.org/10.1088/0034-4885/64/4/203>.
- [87] G. TERASHI, X. WANG, D. PRASAD, T. NAKAMURA, AND D. KIHARA, *DeepMainmast: integrated protocol of protein structure modeling for cryo-EM with deep learning and structure prediction*, Nature Methods, 21 (2024), pp. 122–131, <https://doi.org/10.1038/s41592-023-02099-0>.
- [88] C.-L. TOWSE, S. J. RYSAVY, I. M. VULOVIC, AND V. DAGGETT, *New dynamic rotamer libraries: Data-driven analysis of side-chain conformational propensities*, Structure, 24 (2016), pp. 187–199, <https://doi.org/10.1016/j.str.2015.10.017>.
- [89] B. K. VAINSTEIN AND A. B. GONCHAROV, *Determining the spatial orientation of arbitrarily arranged particles given their projections*, Soviet Physics Doklady, 31 (1986), pp. 278–280. English translation of original paper in Doklady Akademii Nauk SSSR, 287, 1131–1134, 1986.
- [90] M. VARADI, S. ANYANGO, M. DESHPANDE, S. NAIR, C. NATASSIA, G. YORDANOVA, D. YUAN, O. STROE, G. WOOD, A. LAYDON, A. ŽÍDEK, T. GREEN, K. TUNYASUVUNAKOOL, S. PETERSEN, J. JUMPER, E. CLANCY, R. GREEN, A. VORA, M. LUTFI, M. FIGURNOV, A. COWIE, N. HOBBS, P. KOHLI, G. KLEYWEGT, E. BIRNEY, D. HASSABIS, AND S. VELANKAR, *AlphaFold protein structure database: massively expanding the structural coverage of protein-sequence space with high-accuracy models*, Nucleic Acids Research, 50 (2021), pp. D439–D444, <https://doi.org/10.1093/nar/gkab1061>, <http://dx.doi.org/10.1093/nar/gkab1061>.
- [91] C. VÉNIEN-BRYAN AND C. A. H. FERNANDES, *Overview of membrane protein sample preparation for single-particle cryo-electron microscopy analysis*, International Journal of Molecular Sciences, 24 (2023), p. 14785, <https://doi.org/10.3390/ijms241914785>.
- [92] P. VIRTANEN, R. GOMMERS, T. E. OLIPHANT, M. HABERLAND, T. REDDY, D. COURNAPEAU, E. BUROVSKI, P. PETERSON, W. WECKESSER, J. BRIGHT, S. J. VAN DER WALT, M. BRETT, J. WILSON, K. J. MILLMAN, N. MAYOROV, A. R. J. NELSON, E. JONES, R. KERN, E. LARSON, C. J. CAREY, İ. POLAT, Y. FENG, E. W. MOORE, J. VANDERPLAS, D. LAXALDE, J. PERKTOLD, R. CIMRMAN, I. HENRIKSEN, E. A. QUINTERO, C. R. HARRIS, A. M. ARCHIBALD, A. H. RIBEIRO, F. PEDREGOSA, P. VAN MULBREGT, AND SciPy 1.0 CONTRIBUTORS, *SciPy 1.0: Fundamental Algorithms for Scientific Computing in Python*, Nature Methods, 17 (2020), pp. 261–272, <https://doi.org/10.1038/s41592-019-0686-2>.

- [93] R. E. A. WILLIAMS, D. W. MCCOMB, AND S. SUBRAMANIAM, *Cryo-electron microscopy instrumentation and techniques for life sciences and materials science*, MRS Bulletin, 44 (2019), pp. 929–934, <https://doi.org/10.1557/mrs.2019.286>.
- [94] L. YOUNES, *Shapes and Diffeomorphisms*, Springer, 2010, <https://doi.org/10.1007/978-3-642-12055-8>.
- [95] X. ZHANG, B. ZHANG, P. L. FREDDOLINO, AND Y. ZHANG, *CR-I-TASSER: assemble protein structures from cryo-EM density maps using deep convolutional neural networks*, Nature Methods, 19 (2022), pp. 195–204, <https://doi.org/10.1038/s41592-021-01389-9>.
- [96] Z. ZHANG, Y. CAI, B. ZHANG, W. ZHENG, L. FREDDOLINO, G. ZHANG, AND X. ZHOU, *DEMO-EM2: assembling protein complex structures from cryo-EM maps through intertwined chain and domain fitting*, Briefings in Bioinformatics, 25 (2024), p. bbae113, <https://doi.org/10.1093/bib/bbae113>.
- [97] E. D. ZHONG, T. BEPLER, B. BERGER, AND J. H. DAVIS, *CryoDRGN: reconstruction of heterogeneous cryo-EM structures using neural networks*, Nature Methods, 18 (2021), pp. 176–185, <https://doi.org/10.1038/s41592-020-01049-4>.
- [98] N. ZHOU, H. WANG, AND J. WANG, *EMBuilder: A template matching-based automatic model-building program for high-resolution cryo-electron microscopy maps*, Scientific Reports, 7 (2017), p. 2664, <https://doi.org/10.1038/s41598-017-02725-w>.